To the Graduate Council:

I am submitting herewith a thesis written by Janis Keeney-Walker entitled "A Numerical Study of Local Crack-Tip Fields for Modeling Cleavage Fracture Initiation." I have examined the final copy of this thesis for form and content and recommend that it be accepted in partial fulfillment of the requirements for the degree of Master of Science, with a major in Engineering Science.

John D. Landes, Major Professor

We have read this thesis
and recommend its acceptance:

Accepted for the Council:

Vice Provost
and Dean of The Graduate School

STATEMENT OF PERMISSION TO USE

In presenting this thesis in partial fulfillment of the requirements for a Master's degree at The University of Tennessee, Knoxville, I agree that the Library shall make it available to borrowers under rules of the Library. Brief quotations from this thesis are allowable without special permission, provided that accurate acknowledgment of the source is made.

Permission for extensive quotation from or reproduction of this thesis may be granted by my major professor, or in his absence, by the Head of Interlibrary Services when, in the opinion of either, the proposed use of the material is for scholarly purposes. Any copying or use of the material in this thesis for financial gain shall not be allowed without my written permission.

Signature Janis Keeney-Walker

Date 4/17/90

A NUMERICAL STUDY OF LOCAL CRACK-TIP FIELDS FOR MODELING CLEAVAGE FRACTURE INITIATION

A Thesis

Presented for the

Master of Science

Degree

The University of Tennessee, Knoxville

Janis Keeney-Walker

May 1990

ACKNOWLEDGMENTS

I greatly appreciate the loving support and inspiration of my husband, James, family, and friends. Without their patience and encouragement, this thesis could not have been completed. I am indebted to Professors John Landes, Osama Soliman, and Richard Bass, who served as my chairperson and committee, respectively. With their consultation, criticism, and encouragement, I was able to achieve results otherwise impossible. In particular, my sincere appreciation is expressed to Richard Bass for his guidance and his dedication to my development as a student, as a researcher, and as a person. I would also like to recognize the Heavy-Section Steel Technology Program at the Oak Ridge National Laboratory for their support and interest in this project. I gratefully acknowledge Barbara Coppin for her patience and continued friendship for typing draft after draft.

These people have made the pursuit of my Graduate degree both very enjoyable and rewarding.

ABSTRACT

The prediction of cleavage crack initiation in large-scale wide plate (WP) specimens from small (CT) specimens utilizing linear elastic fracture mechanics methodology has not been effective. In the wide-plate tests conducted by the Heavy-Section Steel Technology Program at Oak Ridge National Laboratory, crack initiation has consistently occurred at K_I values ranging from two to four times those predicted by the CT specimens. Studies were initiated to develop crack-tip stress field criteria incorporating effects of geometry, size, and constraint that will lead to improved predictions of cleavage initiation in WP specimens from CT specimens. The work centers around nonlinear 2-D and 3-D finite element analyses of the crack-tip stress fields in these geometries. Analyses were conducted on CT and WP specimens for which cleavage initiation fracture had been measured in laboratory tests. The local crack-tip fields generated for these specimens were then used in the evaluation of fracture correlation parameters to augment the K_I parameter for predicting cleavage initiation. Parameters of hydrostatic constraint and of maximum principal stress, measured pointwise and volumetrically, are included in these evaluations.

The results indicate a potential for correlating the local crack-tip fields with the cleavage initiation process via the maximum principal stress criterion based on achieving a critical cumulative area within a critical stress contour. This criterion has been

successfully applied to correlate cleavage initiation in 2T-CT and WP specimen geometries.

TABLE OF CONTENTS

CHAPTER PAGE

LIST OF TABLES

LIST OF FIGURES

FIGURE PAGE

FIGURE PAGE

CHAPTER 1

INTRODUCTION

Traditionally, fracture mechanics has focused on understanding fracture processes and providing fracture criteria for predicting the failure of structures with defects. In applications of linear elastic fracture mechanics (LEFM) methodology, mode I crack initiation is postulated to occur when the applied stress-intensity factor (K_I) exceeds a critical value (K_{Ic}) determined by material testing of small specimens, i.e., compact (CT) specimens. However, in tests of large-scale single-edge notched tension wide-plate (WP) specimens [1] of A533 grade B class 1 (A533B) steel, conducted by the Heavy-Section Steel Technology (HSST) Program at Oak Ridge National Laboratory (ORNL), cleavage crack initiation occurred at K_I values well above those predicted by the small specimens. In fact, the K_I/K_{Ic} ratios ranged from 2.0 to 4.0. In Fig. 1.1*, wide-plate data from the WP-1 series [1] is shown to be consistently in the upper scatter band of data from CT specimens. Consequently, studies were initiated in the HSST program to develop additional crack-tip stress field criteria incorporating effects of geometry, size, and thickness that will lead to improved predictions of cleavage initiation in reactor pressure vessel (RPV) steels.

---

* All tables and figures can be found in Appendix B.

The work centers around multidimensional analyses of the crack-tip stress fields in small-scale CT and large-scale WP specimens which model specimens previously tested under the HSST Program. All fracture data utilized in the study are measured on specimens taken from a single plate of A533B steel that had been extensively characterized for mechanical and fracture properties. Local crack-tip fields were generated from elastic-plastic analyses of two- and three-dimensional finite element models of these test specimens. The crack-tip fields from these specimen analyses were utilized to evaluate potential correlation parameters that may be used to augment the K_I parameter for predicting cleavage initiation. The correlation parameters examined in this study include the ratio of hydrostatic-to-effective stress, and the magnitude of maximum principal stress evaluated pointwise and volumetrically ahead of the crack tip.

The following chapter summarizes material characterization of the A533B steel source plate for the test specimens. This is followed by a chapter describing the CT and WP testing programs which provided the cleavage fracture toughness data of the present study. Next, a description is given of the candidate cleavage initiation correlation parameters evaluated in this study. This is followed by a detailed description of the posttest fracture analyses of the CT and WP specimens, as well as an assessment of the candidate fracture toughness correlation parameters derived from the local crack-tip fields of the specimens. Finally, recommendations are made concerning the predictive capabilities of a dual parameter model for cleavage initiation toughness in RPV steels.

CHAPTER 2

MATERIAL CHARACTERIZATION

2.1 MATERIAL DESCRIPTION

The first series of wide-plate crack-arrest test specimens [1] and the compact test specimens employed in this study are taken from HSST plate 13A, which is of A533B steel. The 18.7 cm-thick plate (melt C4453) was produced by Lukens Steel Company and has the following chemical composition (wt %): 0.19% C, 1.28% Mn, 0.012% P, 0.013% S, 0.21% Si, 0.64% Ni, and 0.55% Mo. An average grain size of ASTM 7-8 (.032 mm-0.22 mm) was measured for the material. Hardness was found to be 89-91 Diamond Pyramid Hardness (DPH) (average) and did not vary through the thickness of the plate, due to the extended stress relief and tempering treatments to which the material was subjected.

2.2 TENSILE PROPERTIES

Properties of the plate material included Young's modulus E = 206.9 GPa, Poisson's ratio ν = 0.3, thermal expansion coefficient α = 11 x 10^{-6}/°C, and density ρ = 7850 kg/m^3. As can be seen in Fig. 2.1, there was no real variation in room-temperature tensile properties through the plate thickness. The average room-temperature tensile properties (longitudinal orientation) are ultimate tensile strength, 597 MPa; yield strength, 445 MPa; total elongation, 24%; and reduction in area, 69%.

Variations of longitudinal tensile properties with temperature for the plate center are shown in Fig. 2.2. Multilinear representations of the stress-strain curves for the material, with temperature as a parameter, are shown in Fig. 2.3. The temperature-dependent yield stress for the multilinear representations in this figure is given by the function

$$\sigma_y = 374.866 + 59.894e^{-0.0079328T} \quad , \qquad (2.1)$$

where σ_y and T are in megapascals and degrees Celsius, respectively. The stress-plastic-strain modulus H'(T) as a function of temperature is presented in Table 2.1.

2.3 CHARPY V-NOTCH PROPERTIES

Figure 2.4 shows that the Charpy V-notch (CVN) properties in the longitudinal orientation also did not vary appreciably through the plate thickness. The LT orientation has the specimen parallel to the rolling direction and the notch (crack propagation) transverse to the rolling direction, similar to that for the wide-plate crack-arrest specimens. For the center 100 mm of the plate, which was the portion used for the wide-plate testing, the average 41-J transition temperature is -30°C, the 50% ductile transition temperature is 2°C, the upper-shelf energy is 160 J, the onset of upper-shelf energy is 55°C, and 35 mils lateral expansion is obtained at -13°. The RT_{NDT} (ASME reference nil-ductility temperature) was determined to be -23°C, as measured by drop-weight/Charpy testing in the LT orientation.

2.4 FRACTURE TOUGHNESS RESULTS

The fracture-toughness properties of HSST Plate 13A were determined at ORNL using 25.4- and 50.8-mm compact specimens (1T-CT and 2T-CT, respectively) modified for load-line displacement measurement [1]. The single-specimen unloading compliance technique of ASTM 1152 was used to measure crack growth during testing. The specimens were loaded under load-line displacement control at a rate of 0.2 mm/min. When applicable, K_{Ic} values were determined according to ASTM E399. Otherwise, the modified Ernst J-integral was used to infer K_{Ic} values from the relation

$$K_{J_c} = \sqrt{EJ_c} \ , \tag{2.2}$$

where

$$E(GPa) = 207.2 - 0.057\ T\ (°C). \tag{2.3}$$

A plasticity correction ("beta-correction") was determined from the K_J value at cleavage using the Merkle method [2]. A summary of the fracture mechanics tests is provided in Table 2.2. To judge the inherent material variability, upper and lower bounds (two standard deviations from the mean) are shown with the measured data in Figs. 2.5 and 2.6 for the fracture toughness, beta-corrected fracture toughness, and the average tearing modulus. The material tearing resistance is of the form of a power-law J-resistance curve,

$$J_R = c(\Delta a)^m \ , \tag{2.4}$$

where $c = 0.3539$, $m = 0.4708$, and the units of J_R and Δa are megajoules per square meter and millimeters, respectively.

Fracture-toughness relations for crack initiation and arrest have been developed on the basis of small-specimen data and are given as follows:

$$K_{Ic} = 51.276 + 51.897e^{0.036(T - RT_{NDT})} \qquad (2.5)$$

$$K_{Ia} = 49.957 + 16.878e^{0.029(T - RT_{NDT})} \qquad (2.6)$$

Units for K and T are megapascals times square root meters and degrees Celsius, respectively.

CHAPTER 3

WIDE-PLATE TESTING PROGRAM AND TEST DATA

3.1 WP-1 TEST SERIES

The primary objective of the wide-plate crack-arrest studies [1,3-7] is to generate data and associated analysis methods for understanding the crack-arrest behavior of prototypical RPV steels at temperatures near and above the onset of the Charpy upper-shelf region. Program goals include: (1) extending the existing K_{Ia} databases to values above those associated with the upper limit in the American Society of Mechanical Engineers Boiler and Pressure Vessel Code (ASME B&PVC); (2) clearly establishing that crack arrest occurs prior to fracture-mode conversion; and (3) validating the predictability of crack arrest, stable tearing, and/or unstable tearing sequences for RPV materials. Sixteen wide-plate crack-arrest tests have been completed, ten utilizing specimens fabricated from A533B material and six fabricated from a low-upper-shelf base material.

The 1 x 1 x 0.1 m, or 1 x 1 x 0.15 m wide-plate specimens were machined and precracked by ORNL. The precracking was done by hydrogen charging an electron-beam (EB) weld located at the base of a premachined notch in the plate. The initial total crack length, notch depth plus EB weld, for each specimen was nominally 0.2 m (a/W ~ 0.2). Each face of a specimen was grooved to a depth equal to 12.5% of the plate thickness. Starting with the third specimen in test series WP-1 (WP-1.3), the crack front of each specimen, with the exception of specimens WP-2.3 and WP-2.6, was machined into a truncated chevron configuration to reduce the tensile load required to achieve crack initiation. Upon completion of the machining operations, each specimen was shipped to the National Institute of Standards and Technology (NIST) in Gaithersburg, MD, where it was welded to pull plates nominally having the same cross-section geometry as the specimen to produce the test article shown schematically in Fig. 3.1.

To obtain pertinent data during a test, each wide-plate specimen was instrumented with three primary types of devices: (1) thermocouples; (2) strain gages; and (3) crack opening displacement (COD) gages. Also, an acoustic emission transducer was located on the lower pull tab of each specimen. After instrumenting, the specimen was placed into the 27-MN capacity tensile testing machine and electric-resistance strip heaters attached to the back edge of the plate. A temperature gradient was imposed across the plate by spraying liquid nitrogen (LN_2) onto the notched edge while heating the other edge. Generally, the mid-plate ($a/W = 0.5$) temperature was selected to correspond to that of the onset of Charpy upper-shelf energy (USE) for the material tested, and the crack-tip temperature was varied to provide the desired initiation load. Upon obtaining the desired temperature gradient, tensile load was applied to the specimen at a rate which varied from 11 to 312 kN/s, depending on the test, until fracture occurred. Table 3.1 presents a summary of the conditions for testing of the A533B wide-plate materials. A detailed description of each of these tests is provided elsewhere [1,3-7].

Initiation stress-intensity factors obtained from tests in the WP-1 series are compared in Table 3.2. In Fig. 1.1, the WP-1 initiation K_I values are compared with the CT-specimen data from Table 2.2.

3.2 TEST WP-1.2

Results from the second wide-plate test (WP-1.2) were utilized in the cleavage initiation studies described in the following chapters. Testing of specimen WP-1.2 was performed with a crack-tip temperature of -33°C. The cold and hot edges were about -97 and 207°C, respectively, at the approximate time of the crack run-arrest events (Fig. 3.2). The specimen was loaded monotonically at 11 kN/s until fracture occurred at 18.9 MN. Results from a 2-D finite element analysis performed shortly after the test indicated that $K_I = 252$ $MPa \cdot \sqrt{m}$ at initiation. This estimate was also substantially above the estimated K_{Ic} for this material at -33°C ($K_{Ic} \approx 88$ $MPa \cdot \sqrt{m}$; i.e., $K_I/K_{Ic} = 2.86$).

Fractographic analyses of specimen WP-1.2 were conducted after completion of examination of the fracture surface to determine the crack position as a function of time. Figure 3.3 shows the portion of the fracture surface from the EB weld flaw to a point just beyond the second arrest site. The first crack run-arrest event initiated at -33°C and arrested at 62°C. Figure 3.4(a) and (b) shows the Charpy impact and fracture-toughness curves for this material in the same orientation as that of specimen WP-1.2. Note that initiation occurred in the lower transition region, while crack arrest occurred near the onset of Charpy upper-shelf energy. Scanning electron fractographs of two regions of the fracture surface are shown in Figs. 3.5-3.6. Figure 3.5 shows that there was no significant ductile tearing at the first initiation event, while Fig. 3.6 shows that the dominant mode of crack propagation was cleavage.

CHAPTER 4

FRACTURE TOUGHNESS CORRELATION PARAMETERS

The variability in measurement of cleavage fracture toughness of pressure vessel steels (as a function of temperature) is well-documented in the literature (see for example, Refs. [8-14]). As discussed by Merkle [2], this variability can be traced to physical effects, such as difference in size and geometry of test specimens, and to the existence of scatter due to material differences. A large body of literature has developed that examines physical effects based on experimental methods or on micromechanical models [9-11, 15-17], while material variability has been modeled using statistical methods [12-14]. The emphasis in this study is on the resolution of physical effects through the use of correlation parameters based on local crack-tip stress fields. These parameters are described in the following sections.

4.1 HYDROSTATIC CONSTRAINT

As described by Kanninen and Popelar [18], the cleavage fracture model is based on the conditions of small-scale yielding; i.e., the size of the plastic zone ahead of the crack tip is small compared to the K-dominant region and the crack-tip stresses and strains are uniquely characterized by K or J. However, with increasing plasticity, small-scale yielding conditions and K-dominance are eventually lost, and K-values at initiation become size-dependent. Generally, the loss of K-dominance leads to a reduction in triaxiality, which can be quantified conveniently in terms of constraint factors. One type of constraint factor is the ratio of the hydrostatic stress to the von Mises effective stress:

$$h = \sigma_H / \sigma_V \tag{4.1}$$

with

$$\sigma_H = (\sigma_{XX} + \sigma_{YY} + \sigma_{ZZ}) \; / \; 3, \tag{4.2}$$

and

$$\sigma_V = (3 \; (0.5 \; ({\sigma'_{XX}}^2 + {\sigma'_{YY}}^2 + {\sigma'_{ZZ}}^2 + {\sigma_{XY}}^2 + {\sigma_{YZ}}^2 + {\sigma_{XZ}}^2))^{1/2} \tag{4.3}$$

where σ_V is proportional to the square root of the second invariant of the deviatoric stress tensor. A function of this ratio has been used previously by Rice and Tracey [19] to predict macroscopic fracture toughness using microscopic void growth models. A higher value of the constraint factor h indicates a higher degree of triaxiality. When triaxiality is high, the plastic flow of the material decreases, thereby inhibiting the ability of the material to reduce local stress peaks. According to Merkle [2], triaxiality is necessary to sustain cleavage microcrack propagation in normal structural steels because the maximum principal tensile stress must be equal to or greater than the cleavage fracture stress when the maximum principal tensile strain reaches the cracking strain of the grain boundary carbide, which is about 2%.

The hydrostatic stress, and consequently the constraint factor h, in the plastic zone ahead of the crack tip depends on the transverse strain, i.e., the strain parallel to the crack front. For through-cracked specimens such as CT and wide-plate (WP) configurations, the transverse strain depends on the ratio of the plastic-zone size to the thickness. When the plastic zone becomes large compared to the plate thickness, yielding can take place freely in the thickness direction (condition of plane stress). As the transverse contraction strain increases, the maximum hydrostatic stress and the maximum principal tensile stress on the crack plane ahead of the crack tip decreases. Consequently, the load and plastic-zone size at cleavage initiation is increased, with an apparent elevation in the fracture toughness of the material.

4.2 MAXIMUM PRINCIPAL STRESS

In an early study, Richie, Knott and Rice [15] developed a relationship between tensile stress and cleavage fracture toughness in a mild steel under plane strain conditions. In their study, unstable cleavage fracture is postulated to occur when the maximum principal stress exceeds a critical value of stress over a characteristic distance ahead of the crack tip, determined as twice the grain size of the material. The results in Ref. [15] are based on elastic-plastic solutions for the stress distribution ahead of a sharp crack. The use of a sharp-crack model necessitated that the critical stress be achieved over some microstructurally significant distance ahead of the crack tip to avoid predictions of fracture at vanishingly small loads due to the stress singularity.

Merkle [2] asserts that a description of the crack-tip stress and strain fields required to model the onset of cleavage fracture can only be attained by considering the blunting of the crack tip. Crack-tip blunting leads to a finite crack-tip root radius, with zero stress normal to the blunted crack surface. Thus, the point of greatest hydrostatic stress occurs at a small distance ahead of the notch tip, while the greatest strain occurs at the notch tip. Finite deformation analyses performed by McMeeking [20] and McMeeking and Parks [21] indicate the point of maximum stress is approximately $3\delta_t$ ahead of the crack tip, where δ_t is the crack-tip opening displacement. Merkle [2] points out that the blunted crack-tip model eliminates the necessity of exceeding the critical stress over a characteristic distance to cope with a non-existent stress singularity, such as the criterion of Ref. [15]. However, Dodds et al. [17] point out that relaxation of stresses near the free surface of the blunted tip implies that the fracture process zone lies beyond the finitely deforming zone adjacent to the tip. They argue that, because differences in stresses from small-strain and finite deformation analyses of the small-scale yielding model become insignificant beyond $3\delta_t$ from the crack tip, small-strain solutions are adequate to assess crack-tip fields for the stress-controlled cleavage process.

In recent studies, Anderson and Dodds [16] and Dodds et al. [17] constructed a correlation procedure to remove the geometry dependence of cleavage fracture toughness values for single-edge-notched bend (SENB) specimens of A36 steel for a range of crack depths. This procedure utilizes a local stress-based criterion for cleavage fracture and detailed plane-strain finite element analysis. From Ref. [16], dimensional analysis for small-scale yielding implies that the principal stress ahead of the crack tip can be written as

$$\frac{\sigma_1}{\sigma_o} = h \left(\frac{J^2}{\sigma_o{}^2 A} \right) \tag{4.4}$$

or

$$\frac{\sigma_1}{\sigma_o} = g \left(\frac{J}{\sigma_o r} , \theta \right) \tag{4.5}$$

where σ_o is the 0.2% offset yield strength, σ_1 is the maximum principal stress at a point, r and θ are cylindrical coordinates measured from the crack tip, and A is the area enclosed by the contour where σ_1 is a constant. The strategy employed in Ref. [16] utilizes a fracture criterion dependent upon achieving a critical cumulative volume $V(\sigma_1)$ where the principal stress is greater than σ_1. For a specimen subjected to plane strain conditions, the volume is equal to the specimen thickness B times the cumulative area on the mid-plane ($V = BA$). Thus Eq. (4.4) is the appropriate normalization for small-scale yielding solutions when using the latter fracture criterion based on volume or area. In Ref. [17], unstable fracture is defined to occur when the maximum principal stress on the crack plane at $r = k\delta_t$ reaches a critical value, where k is a constant scaling factor. In the study [17], it is shown that the stress fields scale identically with the macroscopic loading parameters (J, δ_t) over the region $4 < k < 8$. Results in both studies [16-17] are normalized with small-scale yielding solutions generated from detailed plane-strain finite element solutions for Ramberg-Osgood material models having values of $n = 5$, 10, and 50 and $\alpha = 1.0$. These solutions are approximated by functions constructed to fit values of the SSY opening-mode stress (σ_{yy}) which have the form

$$\sigma_{yy} = \sigma_0 a \beta^b e^{c\beta} \tag{4.6}$$

where

$$\beta = r/(J/\alpha\sigma_0\epsilon_0) \tag{4.7}$$

and a, b, and c are parameters given in Fig. 4.1, which is reproduced from Ref. [17]. In Fig. 4.1, the SSY solution, Eq. (4.6), is compared with the HRR solution for n = 10.

4.3 APPLICATIONS

In the following, correlations are developed between local crack-tip fields in CT and WP specimens utilizing parameters discussed in this section. Specifically, these include a comparison of the hydrostatic constraint factor, h, for the various loading conditions; imposition of a pointwise maximum principal stress criterion, σ_1 equal a constant, at $r / \delta_t = k$; and a volumetric (or area) maximum principal stress criterion,based on volume $V(\sigma_1)$ (or area $A(\sigma_1)$) and a critical stress σ_1. The results from the maximum principal stress criterion are scaled utilizing the small-scale yielding solution of Eq. (4.6). These criteria are applied to analysis results from both two- and three-dimensional finite element models of CT and WP specimen geometries that were tested in the HSST Program.

CHAPTER 5

POSTTEST ANALYSES AND EVALUATION OF LOCAL CRACK-TIP FIELDS

Two-dimensional (2-D) plane stress/strain and fully three-dimensional (3-D) finite element models were employed to generate the local crack-tip fields for the CT and WP specimens. The numerical analysis techniques utilized both small- and large-strain formulations and the constitutive model representation for A533B steel described in Chapter 2. In the following, detailed descriptions of these models are given, as well as the loading conditions for each analysis performed. Interpretations of the results are discussed in terms of the fracture correlation parameters of Chapter 4, which are evaluated from the local crack-tip fields of the finite element analyses. Procedures for finite element model generation and for evaluation of the J-integral as a function of loading conditions are discussed in Appendix A.

5.1 FINITE ELEMENT MODELS

The 2-D finite element model of the CT configuration used in the nonlinear elastic-plastic analyses consists of 1852 nodes and 580 eight-noded isoparametric elements as shown in Fig. 5.1. Collapsed-prism elements surround the crack tip to allow for blunting and for a $1/r$ singularity in the strains at the crack front. The radial dimension of the collapsed-prism elements at the crack tip is $r = 0.22$ mm ($r/w = 0.0043$) for the 1T-CT specimen and $r = 0.44$ mm ($r/w = 0.0043$) for the 2T-CT specimen.

The 3-D finite element models of the CT specimens were generated by projecting the planform of a 2-D mesh for each specimen through the thickness, using four elements in the thickness direction. The 3-D finite element models of the 1T- and 2T-CT specimens consists of 6344 nodes, 1088 twenty-noded isoparametric brick elements, and 112 collapsed prism elements at the crack front for a 1/r singularity. One quarter of the specimen is modeled due to symmetry. The model for the 2T-CT specimen is shown in Fig. 5.2.

The 2-D finite element model for the WP specimen, WP-1.2, employs 1164 nodes and 348 eight-noded isoparametric elements. The collapsed-prism elements at the crack tip have radial dimensions of $r = 0.375$ mm ($r/w = 0.000375$). The 3-D finite element model of the WP specimen, WP-1.2, consists of 7542 nodes, 1297 twenty-noded isoparametric brick elements, and 112 collapsed prism elements at the crack front. The WP model is shown in Fig. 5.3; a detailed plot of the crack-tip region is given in Fig. 5.4. For the 3-D model, the radial dimension of the collapsed-prism crack-tip elements is $r = 0.75$ mm ($r/w = 0.00075$), which is twice that for the 2-D model.

5.2 FINITE ELEMENT RESULTS AND EVALUATIONS OF CRACK-TIP FIELD PARAMETERS

5.2.1 HYDROSTATIC CONSTRAINT PARAMETER

Two-dimensional plane stress and plane strain analyses were performed using the 2T-CT specimen model and the multilinear true stress-strain curves from Fig. 2.3, assuming uniform temperatures of -150°C, -75°C, and -18°C. A material-nonlinear-only (MNLO) formulation (small-strain theory) was used in these analyses. The load was applied incrementally in the form of a cosine function to the load pin hole up to the load where crack initiation took place for each 2T-CT test. By comparing the plane strain and plane stress solutions for load vs displacement, it was observed that the experimental data relates closely to plane strain formulations (see Fig. 5.5). The constraint factor h given by Eqs. (4.1)-(4.3) was evaluated ahead of the crack tip at the highest initiation load for each of the three temperatures and the results are given in Fig. 5.6. Average values computed for the range of temperatures were h = 2.12 for plane strain and h = 0.62 for plane stress. The plane stress values were very close for all three temperatures but the plane strain value for h at -150°C was lower than expected. This could be due to the lower loads for the tests at -150°C. The maximum K achieved at -150°C was 58.4 MPa$\cdot\sqrt{m}$, as opposed to a K of 143.6 MPa$\cdot\sqrt{m}$ at -75°C.

For the 3-D models of the CT specimens, elastic-plastic static analyses were performed at temperatures of -150°C for the 2T-CT specimen and -75°C for the 1T- and 2T-CT specimens. A MNLO formulation with a multilinear true stress-strain curve was used for the 1T-CT specimen analysis. As there had been some question concerning whether to use small-strain or large-strain theory for these analyses, two analyses were performed for the 2T-CT specimens at -75°C utilizing MNLO and updated lagrangian (UL) formulations (large-strain theory) with a bilinear true stress-strain curve. Figure 5.7 shows the variation of h with the distance from the crack tip at -75°C. All the 3-D analyses fell on the 2-D plane strain curve. For the MNLO analysis, it was observed that the value for h increases steeply toward the crack tip; for the UL analysis, the value of h begins to decrease after a maximum at about 0.4 mm (~ 4 δ_t) from the crack tip. Similar trends were reported in Ref. [22].

A thermo-elastic-plastic analysis of the 3-D WP model was carried out using a MNLO formulation and bilinear true stress-strain curves constructed from the multilinear curves of Fig. 2.3. Boundary conditions prescribed for the model also included the thermal gradient across the plate. In Fig. 5.8, the lower values of h for the WP analysis implies less constraint for the WP than for the CT specimen. However, these values are still considered to be in the plane strain range. When h is plotted through the thickness for both specimens (Fig. 5.9), the values at comparable r's would be slightly lower for the WP specimen than the CT specimen if the side-grooved region of the WP specimen is excluded. The side-groove of the WP specimen gives rise to stress peaks since it was modeled without a finite root radius. In the CT specimen, h is a maximum at center plane and decreases to the 2-D plane stress value at the free surface. When the through-thickness average value, h_m, is plotted versus the stress-intensity factor (Fig. 5.10), constraint is higher for the WP specimen until $K \approx 25$ MPa$\cdot\sqrt{m}$, where h_m reaches a plateau; h_m for the CT specimens continues to increase beyond this point until $K \approx 100$ MPa$\cdot\sqrt{m}$. These results are similar to those observed in Ref. [22] for the CT specimens.

5.2.2 MAXIMUM PRINCIPAL STRESS FRACTURE CRITERIA

The fracture model described in Chapter 4, which is based on maximum principal stress theory, was applied to the analyses of the CT and WP specimens. In applications of the theory, the finite element results are normalized using the small-scale yielding (SSY) analysis of Dodds, et al. described in Ref. [17]. To apply this SSY analysis to the A533B pressure vessel steel of the present study, Ramberg-Osgood parameters of $n = 8.3$ for temperatures of -75°C and -33°C and $n = 8.6$ for a temperature of -18°C were calculated according to procedures described in Ref. [17]. The parameter α was set to 1.0. Values of the parameters a, b, and c in the curve fit function of Eq. (4.6) for the opening-mode stress, σ_{yy}, were then interpolated in the table in Fig. 4.1.

In the first application of the maximum principal stress criterion, the stress σ_{p1} was evaluated on the crack plane at a distance of $r = k\delta_t$ ahead of the crack tip, where k is a constant satisfying $4 \leq k \leq 53$. In Table 5.1, a portion of these results are tabulated for $k = 4$ for the 2-D and 3-D finite element models of the CT and WP specimens. Values of σ_{p1}, J-integral, CTOD, and r are given in Table 5.1 as a function of increasing load, along with the SSY value of J-integral, J_{SSY}, for the corresponding stress level at $r = 4\delta_t$. Analysis results are presented for the 2-D model of the 2T-CT specimen corresponding to test temperatures of -75°C and -18°C. Each of the J values for the 2T-CT specimens in Table 5.1 represents an initiation point in the test series. At -75°C, the σ_{p1} stress increases slightly over the range of loading, with an average value of $\sigma_{p1} = 1410$ MPa.

The lower averaged value of σ_{p1} = 1334 MPa at -18°C is related to the decrease in yield stress with increasing temperature as indicated in Fig. 2.2.

For the 2-D model of the WP specimen, analysis results are given for material stress-strain curves corresponding to temperatures of -75°C and -33°C; the latter temperature represents the crack-tip temperature measured at initiation in wide-plate test WP-1.2. The σ_{p1} stress for both analyses increases slightly with loading, with the exception of the last point where r > 0.8 at -33°C. For the WP specimen, the σ_{p1} stress varies slightly about an average value of 1332 MPa at -75°C and 1265 MPa at -33°C.

As indicated in Table 5.1, the 3-D analyses of the 1T-CT specimen at -75°C and the WP specimen at -33°C both exhibit monotonically decreasing σ_{p1} values with increasing load. The average stress value for the 1T-CT specimen is σ_{p1} = 1400 MPa, while the WP specimen has an average value of σ_{p1} = 1406 MPa. It is observed that there is a significant variation of average σ_{p1} stress between the 2-D plane strain and the 3-D analyses of the WP specimen, a point which is discussed further in the following section.

In Fig. 5.11(a), the normalized σ_{p1} stresses from the 2-D analyses of the 2T-CT specimen at -75°C and -18°C are plotted against normalized distance ahead of the crack tip for a range of applied J values. The stresses are normalized by values from the SSY model loaded to the same value of J. Analogous results are given in Figs. 5.11(b)-(c) for the WP specimen analyses carried out for temperatures of -75°C and -33°C, respectively. For the CT specimen analyses, the normalized stresses increase with normalized distance ahead of the crack tip, but are relatively insensitive to J over the range of initiation loads (Fig. 5.11(a)). Normalized stresses for the WP specimen (Figs. 5.11(b)-(c)) also increase with increasing normalized distance, but decreases appreciably with increasing applied J. Note that the unnormalized value of stress does not decrease with increasing load. The decrease in normalized stress for the WP specimen implies a progressive loss of in-plane constraint due to the developing plastic zone.

Figure 5.12 depicts the relationship between the normalized J-integral from the 2-D analysis of the WP specimen with that from SSY conditions which produce an equivalent opening-mode stress ahead of the crack tip. The dashed line in the figure represents the SSY limit defined by $J_{WP} = J_{SSY}$. The J values are normalized by the crack depth, a, and the flow stress of $\sigma_f = 587$ MPa for A533B steel at -75°C and $\sigma_f = 551$ MPa at -33°C. The result in Fig. 5.12 again illustrates the progressive departure of the WP solution from SSY conditions with increasing load.

As discussed in Chapter 4, an alternative criterion for plane-strain fracture is based upon achieving a critical cumulative area $A(\sigma_1)$, where the maximum principal stress is greater than σ_1. The latter criterion was applied to the analyses of the CT and WP specimens and a portion of the results are summarized in Table 5.2. A maximum principal stress of $\sigma_{p1} = 1400$ MPa was used to generate the contour areas in Table 5.2. This critical stress is based on the average maximum principal stress calculated for the 2-D and 3-D analyses of the

CT specimens in Table 5.1. Also, Hahn et al. [23] estimated that the cleavage microcrack propagation stress for individual grains of ferrite is 1380 MPa. In Table 5.2, the area within the stress contour $\sigma_{p1} = 1400$ MPa is tabulated as a function of load for the 2-D and 3-D finite element solutions. When these areas are normalized with respect to the factor $(\sigma_0/J)^2$, the normalized values vary slightly for the 2T-CT specimen over the range of loading. By contrast, the normalized results for the WP specimen decrease significantly with increasing load, indicating loss of constraint with respect to small-scale yielding.

In the 2-D analyses of the CT specimens, the cumulative area corresponding to the smallest initiation load (0.144 MN) is given by $A_{crit} = 0.0658$ mm^2. Comparing this with the area from the WP analysis at -33°C (crack-tip temperature of test WP-1.2), the same critical area is achieved at an applied load of approximately 15.7 MN; the cumulative area corresponding to the initiation load (18.9 MN) in test WP-1.2 is 0.1226 mm^2. In Fig. 5.13, the applied J values calculated from the 2-D analyses for the 2T-CT and WP specimens are plotted versus the cumulative area within the critical stress contour, $\sigma_{p1} = 1400$ MPa, at each load step. For given values of cumulative area, A, and temperature, T, values of the J-integral for the WP specimen lie above those for the CT specimen, reflecting the differences in crack-tip constraint in these two geometries. Also, for each specimen, and a given value of A, J-integral values increase with temperature due to decreasing yield stress. Using the critical area from initiation values for the 2T-CT specimen at -75°C and -18°C, a prediction can be made for J at initiation of WP-1.2. From the CT specimen results, the predicted A values at initiation for -75°C and -18°C are A = 0.117 mm^2 and 0.144 mm^2, respectively. This implies that the J value at initiation for the WP specimen with a crack-tip temperature of -33°C should lie in the interval (0.233,0.255) MJ/m^2; the calculated J value at initiation for WP-1.2 was 0.244 MJ/m^2.

Cumulative areas within the σ_{p1} = 1400 MPa contour from the 3-D analyses of the 1T-CT specimen and the WP specimen cannot be reconciled with the corresponding 2-D analysis results. As described in the following section, this discrepancy is probably related to mesh refinement and numerical difficulties associated with the 3-D finite element models used in the present study.

5.3 DISCUSSION OF RESULTS

Based upon the analysis results presented in this chapter, several observations can be made concerning the interpretations of local crack-tip fields using the fracture correlation parameters described in Chapter 4. To begin with, comparisons of hydrostatic constraint factors computed from both the 2-D and 3-D analyses of CT and WP specimens indicate that constraint at the mid-plane is lower for the WP specimen, but still in the plane strain range (see, for example, Fig. 5.8). Furthermore, the average constraint factor for both the CT and WP geometries varies only moderately over the range of applied loads considered in the analyses (See Fig. 5.10). Consequently, due in part to this relative insensitivity to loading, it was not possible to use hydrostatic constraint as a parameter to correlate J values at initiation in these geometries.

Difficulties were also encountered with the maximum principal stress criterion for initiation based on achieving a critical stress at a fixed normalized distance ahead of the crack tip. From Table 5.1, the σ_{p1} stress computed at $r/\delta_t = 4$ for the 2-D WP analysis at -75°C remains significantly below that calculated for the 2T-CT specimen at the same temperature over the range of loading shown in the table. Similarly, the σ_{p1} stress values for the WP specimen at -33°C remained below those for the 2T-CT specimen analyzed at -18°C. The stresses from the 3-D analysis of the 1T-CT specimen at -75°C covered the same range as the stresses from the 2-D analysis of the 2T-CT specimen at the same temperature. However, the 3-D analysis of the WP specimen yielded stresses that did not correspond with the 2-D plane strain results for a temperature of -33°C. The difficulty with the 3-D analysis of the WP specimen appears to be one of finite element modeling. For $r/\delta_t = 4$, the values of r and σ_{p1} were typically interpolated between the Gauss points of the innermost ring of elements in the 3-D model; a 2 x 2 x 2 Gauss point rule was employed. An extra ring of elements was included at the crack tip of the 2-D model and a 3 x 3 Gauss point rule was adopted. Thus, the peak crack-tip stresses were better represented in the 2-D analysis.

The maximum principal stress criterion based on achieving a critical cumulative area within a critical stress contour appears to offer promise for interpreting cleavage initiation in terms of local crack-tip fields. The 2-D analyses of the 2T-CT specimens at -75°C and at -18°C provide contour areas corresponding to initiation that are consistent with the values calculated from the 2-D model of the WP specimen at -33°C. It is probable that these estimates could be further refined with analyses based on improved modeling of the crack-tip zone.

Cumulative areas calculated from the 3-D models of the CT and WP specimens cannot be reconciled with the 2-D analysis results. Again, the difficulties stem from lack of sufficient mesh refinement in the crack-tip area. It can be observed in Fig. 5.14 from Ref. [17] that the contour for $\sigma_1/\sigma_0 = 3.2$ extends approximately 0.148 mm from the crack plane. The 3-D model for the WP specimen shown in Fig. 5.15, at the time of initiation, has a contour for $\sigma_{p1} = 1460$ MPa contained just in the first ring of elements to the right of the crack tip (an element length of 0.75 mm). This severely limits an accurate volume or area calculation. Clearly, if constraint conditions are to be incorporated through 3-D modeling of the crack-tip region, then greater mesh refinement will be required to achieve accurate representation of the local crack-tip fields.

CHAPTER 6

SUMMARY AND CONCLUSIONS

Elastic-plastic 2-D and 3-D finite element analyses of CT and WP specimens of A533B steel were carried out to correlate selected local crack-tip parameters with measured cleavage initiation loads. Results of the study can be summarized as follows:

1. Comparisons of the hydrostatic constraint factor evaluated from the CT and WP specimen solutions indicate that mid-plane constraint is lower for the WP specimen and varies only moderately over the range of applied loads for both geometries. It was not possible to use the hydrostatic constraint as a factor to correlate J values at initiation in the two geometries due to the insensitivity of h to loading.

2. Application of the maximum principal stress criterion for initiation based on achieving a critical stress at a fixed normalized distance ahead of the crack tip did not produce a viable correlation between the 2-D analyses of the CT and WP specimens. A more positive result may be achieved for this criterion by employing finite element models with improved crack-tip mesh refinement.

3. The maximum principal stress criterion based on achieving a critical cumulative area within a contour of critical stress successfully correlated the cleavage initiation load in wide-plate test WP-1.2 with measured values from the 2T-CT specimen tests. By plotting applied J values for the small- and large-specimens versus the

cumulative area within a critical stress contour, one can predict the initiation J for the large-specimen from the critical areas attained by the small-specimens at initiation. In effect, these cumulative areas and J values are used as a two parameter model for predicting cleavage initiation in the larger structure. These results were obtained using 2-D plane strain analyses of the two specimen geometries. It is anticipated that further improvement in the correlation is possible with more refined finite element models.

4. Analysis results from the 3-D models of the CT and WP specimens cannot be reconciled with the 2-D analysis results. Clearly, these difficulties stem from lack of sufficient mesh refinement (both in-plane and thru-thickness) in the crack-tip region of the 3-D models.

Results from this study indicate that the future focus should be on detailed 2-D plane strain elastic-plastic analyses of the CT and WP geometries. It was observed that important results can be obtained from 2-D analyses without the excessive computing resource requirements of 3-D analyses. Highly refined meshes at the crack tip are required to accurately compute the cumulative areas for the maximum principal stress criterion. Based on values of cumulative area and applied J, the two-parameter model could be tested further to establish its transferability between laboratory specimens and engineering structures for predicting cleavage initiation.

LIST OF REFERENCES

1. Naus, D. J., Bass, B. R., Pugh, C. E., Nanstad, R. K., Merkle, J. G., Corwin, W. R., and Robinson, G. C., Crack-Arrest Behavior in SEN Wide Plates of Quenches and Tempered A533 Grade B Steel Tested Under Non-Isothermal Conditions, NUREG/CR-4930 (ORNL-6338), Martin Marietta Energy Systems, Inc., Oak Ridge National Laboratory, August 1987.

2. Merkle, J. G., An Examination of the Size Effects and Data Scatter Observed in Small-Specimen Cleavage Fracture Toughness Testing, NUREG/CR-3672 (ORNL/TM-9088), Martin Marietta Energy Systems, Inc., Oak Ridge National Laboratory, April 1984.

3. Naus, D. J., Bass, B. R., Keeney-Walker, J., Fields, R. J., deWit, R., and Low, S. R., Summary of HSST Wide-Plate Crack-Arrest Tests and Analyses, NUREG/CP-0091, Vol. 2, Materials Engineering/ Pressure Vessel Research, Proceedings of United States Nuclear Regulatory Commission Fifteenth Water Reactor Safety Information Meeting, Gaithersburg, MD, February 1988.

4. Naus, D. J., Bass, B. R., Keeney-Walker, J., Fields, R. J., deWit, R., and Low, S. R., HSST Wide-Plate Test Results and Analysis, NUREG/CP-0097, Vol. 2, Materials Engineering/Pressure Vessel Research, Proceedings of United States Nuclear Regulatory Commission Sixteenth Water Reactor Safety Information Meeting, Gaithersburg, MD, March 1989.

5. Naus, D. J., Keeney-Walker, J., Bass, B. R., Fields, R. T., deWit, R., and Low III, S. R., High Temperature Crack-Arrest Behavior of Prototypical and Degraded (simulated) Reactor Pressure Vessel Steels, International Journal of Pressure Vessels & Piping 39, pp. 189-208, 1989.

6. Naus, D. J., Keeney-Walker, J., Bass, B. R., Bolt, S. E., Field, R. J., deWit, R., and Low III, S. R., High-Temperature Crack-Arrest Behavior in 152-mm-Thick SEN Wide Plates of Quenched and Tempered A533 Grade B Class 1 Steel, NUREG/CR-5330 (ORNL/TM-11083), Martin Marietta Energy Systems, Inc. Oak Ridge National Laboratory, April 1989.

7. Pugh, C. E., Bass, B. R., Naus, D. J., Nanstad, R. K., deWit, R., Fields, R. J., and Low III, S. R., Crack Run-Arrest Behavior in Wide SEN Plates of a LWR Pressure Vessel Material, Paper G1/4, Transactions of the 9th International Conference on Structural Mechanics in Reactor Technology, pp. 21-26, 1987.

8. Irwin, G. R., The Effect of Size Upon Fracturing, in Symposium on Effect of Temperature on the Brittle Behavior of Materials with Particular Reference to Low Temperatures, ASTM STP 158, American Society for Testing Materials, pp. 176-194, 1954.

9. Irwin, G. R., Fracture Mode Transition for a Crack Traversing a Plate, J. Basic Eng. 82(2), pp. 415-425, 1960.

10. Pisarski, H. G., Influence of Thickness on Critical Crack Opening Displacement (COD) and J. Values, Int. J. Fract. 18(4), pp. 427-440, August 1981.

11. Chell, G. G., and Curry, D. A., Mechanics and Mechanisms of Cleavage Fracture, Chap. 3 in Developments in Fracture Mechanics - 2, ed. G. G. Chell, Applied Science Publishers, London, 1981.

12. Landes, J. G., and Shaffer, D. H., Statistical Characterization of Fracture in the Transition Region, Fracture Mechanics: Twelfth Conference, ASTM STP 700, American Society for Testing and Materials, pp. 368-382, 1980.

13. Andrews, W. R., Kumar, V., and Little, M. M., Small-Specimen Brittle-Fracture Toughness Testing, Fracture Mechanics: Thirteenth Conference, ASTM STP 743, American Society for Testing and Materials, Philadelphia, PA, pp. 476-598, 1981.

14. Rosenfield, A. R., and Shetty, D. K., Cleavage Fracture in Steel in the Ductile-Brittle Transition Region, paper presented at the ASTM Symposium on Users' Experience with Elastic-Plastic Fracture Toughness Test Methods, Louisville, Ky., April 1983.

15. Ritchie, R. O., Knott, J. F., and Rice, J. R., On the Relationship Between Critical Tensile Stress and Fracture Toughness in Mild Steel, Journal of Mechanics and Physics of Solids, Vol. 21, pp. 395-410, 1973.

16. Anderson, T. L., Dodds Jr., R. H., Specimen Size Requirements for Fracture Toughness Testing in the Transition Region, submitted to Journal of Testing and Evaluation.

17. Dodds Jr., R. H., Anderson, R. L., Kirk, M. T., A Framework to Correlate a/W Ratio Effects on Elastic-Plastic Fracture Toughness (Jc), submitted to International Journal of Fracture.

18. Kanninen, M. R., and Popelar, C. H., Advanced Fracture Mechanics, Oxford University Press, New York, New York, 1985.

19. Rice, J. R., and Tracey, D. M., On the Ductile Enlargement of Voids in Triaxial Stress Fields, Journal of the Mechanics and Physics of Solids, Vol. 17, pp. 201-217, 1969.

20. McMeeking, R. M., Finite Deformation Analysis of Crack-Tip Opening Elastic-Plastic Materials and Implications for Fracture, Journal of the Mechanics and Physics of Solids, Vol. 26, pp. 357-381, 1977.

21. McMeeking, R. M., and Parks, D. M., On the Criteria for J-Dominance of Crack-Tip Fields in Large-Scale Yielding, Elastic-Plastic Fracture, ASTM STP 668, American Society for Testing and Materials, pp. 175-197, 1979.

22. Kordisch, H., Sommer, E., and Schmitt, W., The Influence of Triaxility on Stable Crack Growth, Nuclear Engineering and Design, 112, pp. 27-35, 1989.

23. Hahn, G. T., Gilbert, A., and Reid, C. N., Model for Crack Propagation in Steel, J. Iron Steel Inst. (London) 202, pp. 677-684, August 1964.

APPENDIXES

APPENDIX A

THE ORMGEN/ORVIRT FRACTURE ANALYSIS SYSTEM

THE ORMGEN/ORVIRT FRACTURE ANALYSIS SYSTEM

The two- and three-dimensional finite element analyses described in Chapter 5 were performed using a modified version of the ORNL-developed ORMGEN/ORVIRT [1, 2] fracture analysis system and the ADINA [3] general purpose finite element program. A brief description of the ORMGEN/ORVIRT system and of modifications of the system required for the present study are given below.

A.1 THE ORMGEN-3D FINITE ELEMENT MESH GENERATOR

Program ORMGEN-3D automatically generates a fully 3-D finite element model for plate and cylinder geometries containing cracks. In general, one-eighth or one-quarter of the structure is modeled, depending upon the configuration or option selected. The strategy employed in the program is to surround the crack front with a core of special crack-tip elements (see Fig. A.1) and to model the remainder of the structure with conventional twenty-noded isoparametric brick elements. Element group I of the finite element model consists of the inner core of special crack-tip elements enclosed by one or more layers of conventional brick elements (Fig. A.1). Eight element divisions are used in a plane orthogonal to the crack front, while the number of element divisions along the arc length of the crack front is user-specified (see Fig. A.1). The remaining conventional brick elements of the model constitute element group II.

The special crack-tip elements are employed along the crack front to model the appropriate singularity in the stress field. For linear elastic calculations, the quarter-point wedge element on Fig. A.2 (a) is used at the crack front to allow for a $1/\sqrt{r}$ singularity in the stress and strain fields, where r is the radial distance from the crack tip. Figure A.2 (b) illustrates the collapsed prism element appropriate for a perfectly plastic material, with midside nodes that allow for a 1/r singularity at the crack front. In the collapsed element, the nodes that initially share the same locations at the tip will separate with increasing load to allow for blunting of the crack (see Fig. A.3). The program allows the user to select either of the two special crack-tip elements, depending upon whether the application is for linear elastic fracture analysis or for ductile fracture analysis.

For geometric parameters specified by the user, the program generates an appropriate mesh in the crack plane (always the X-Y plane), which is then translated, rotated or distorted to compatible shapes in other planes of the model. The program automatically allows for coarser modeling in regions remote from the crack front. Output from the program is written to specified disk I/O data sets using an ADINA-compatible format.

For purposes of this study, a module was developed and installed in ORMGEN that generates 3-D finite-element models of prismatic bodies (such as the CT and WP specimens of Section 5) from any 2-D finite element mesh. The module is also capable of incorporating side grooves into the 3-D model.

A.2 THE ORVIRT FRACTURE MECHANICS PROGRAM

Computational methods in fracture mechanics have focused increasingly on energy release rate techniques for computing stress-intensity parameters of crack configurations. A method well suited for 3-D calculations is the virtual-crack-extension technique. DeLorenzi [4] used the virtual extension method and continuum theory to devise an analytical expression for the energy release rate that is not tied to a particular numerical technique. In applications, deLorenzi [5, 6] used the finite element method to evaluate the energy release rate function.

Certain studies of fracture phenomena, such as those associated with pressurized-thermal-shock, require that crack-tip stress-intensity parameters be determined for cracked structures subjected to combined thermal and mechanical loads. Bass and Bryson [7] modified the isothermal formulation of deLorenzi to account for thermal strains in cracked bodies and implemented the resultant formulation in the ORVIRT program. In Ref. [7], the method requires calculation of the released energy G* corresponding to a small crack advance in a cracked body subjected to surface tractions F_α, body force f_α, and temperature distribution T (see Fig. A.4). Points of configuration I (prior to crack advance) are mapped into configuration II (after crack advance) by the mapping

$$\bar{x}_\alpha = x_\alpha + \Delta x_\alpha(x_\beta) \quad , \tag{A.1}$$

where $x_\alpha, \bar{x}_\alpha$ correspond to coordinates in configurations I, and II, respectively, and Δx_α is the incremental change in coordinates. From Refs. [4,7], the total energy release rate G_T is given by

$$G_T = G^*/\Delta A \tag{A.2}$$

where ΔA is the area increment covered by the virtual extension of the crack front (see Fig. A.5), and

$$\begin{aligned} G^* = & \int_V \left(\sigma_{\alpha\beta} \frac{\partial u_\alpha}{\partial x_\delta} - W\delta_{\delta\beta} \right) \frac{\partial \Delta x_\delta}{\partial x_\beta} \quad dV \\ & + \int_V \left(\sigma_{\alpha\beta} \frac{\partial \Theta_{\alpha\beta}}{\partial x_\delta} - f_\alpha \frac{\partial u_\alpha}{\partial x_\delta} \right) \Delta x_\delta dV \end{aligned} \tag{A.3}$$

In Eq. A.3, $\sigma_{\alpha\beta}$ are the components of the stress tensor, u_α are displacement components, $\Theta_{\alpha\beta}$ are the strains of free thermal expansion, x_δ are spatial coordinates, and dV is the volume differential. The strain energy density W is given by

$$W = \int_0^{\epsilon'_{\gamma\delta}} \sigma_{\alpha\beta} d\epsilon'_{\alpha\beta} \quad , \quad \epsilon'_{\alpha\beta} = \epsilon_{\alpha\beta} - \Theta_{\alpha\beta} \tag{A.4}$$

where the mechanical strain components $\epsilon'_{\alpha\beta}$ are defined in terms of the total strains $\epsilon_{\alpha\beta}$ and the thermal strains $\Theta_{\alpha\beta}$.

More recently, Moran and Shih [8] have described an expression for energy flow to the crack tip, G_T, which does not assume a particular constitutive model,

$$G^* = - \int_V \left(W\delta_{\delta\beta} - \sigma_{\alpha\beta} \frac{\partial u_\alpha}{\partial x_\delta} \right) \frac{\partial \Delta x_\delta}{\partial x_\beta} \, dV \tag{A.5}$$

$$- \int_V \left(\frac{\partial W}{\partial x_\alpha} \delta_{\beta\alpha} - \left(\sigma_{\alpha\delta} \frac{\partial u_\alpha}{\partial x_\beta} \right)_{,\delta} \right) \Delta x_\beta \, dV$$

In Eq. (A.5), W must be interpreted as the strain-history dependent stress-work density. It can be shown that Eq. (A.5) reduces to the form given by Eq. (A.3) for linear elastic and nonlinear elastic material response.

For purposes of this study, the modified formulation for G* given by Eq. (A.5) was implemented in the ORVIRT program, along with other modifications for evaluating local crack-tip constraint parameters described in Chapter 4. The ORVIRT program functions as a postprocessor of a conventional finite element solution obtained from the ADINA program. The functional G* of Eqs. (A.3) or (A.5) is evaluated numerically from solution data written to the nodal-point and element portholes of ADINA and from a user-supplied virtual extension (Δx_β) of the crack front. Average and local values of G_T are evaluated, respectively, from uniform and local virtual extensions of the crack front (see Fig. A.5). A more complete description of ORVIRT is given in Ref. [2].

REFERENCES

1. Bass, B. R. and Bryson, J. W., Applications of Energy Release Rate Techniques to Part-Through Cracks in Plates and Cylinders, Volume 1, ORMGEN-3D: A Finite Element Mesh Generator for 3-Dimensional Crack Geometries, NUREG/CR-2997/V1, (ORNL/TM-8527), Oak Ridge National Laboratory, Oak Ridge, TN, December 1982.

2. Bass, B. R. and Bryson, J. W., Applications of Energy Release Rate Techniques to Part-Through Cracks in Plates and Cylinders, Volume 2, ORVIRT: A Finite Element Program for Energy Release Rate Calculations for 2-D and 3-D Crack Models, NUREG/CR-2997/V2 (ORNL/TM-8527), Oak Ridge National Laboratory, Oak Ridge, TN, February 1983.

3. Bathe, K. J., ADINA - A Finite Element Program for Automatic Dynamic Incremental Nonlinear Analysis, Massachusetts Institute of Technology Report 82448-1 (1975, revised 1978).

4. DeLorenzi, H. G., On the Energy Release Rate and the J-Integral for 3-D Crack Configurations, General Electric TIS Report 80CRD113, 1980.

5. DeLorenzi, H. G., and Shih, C. F., 3-D Elastic-Plastic Investigation of Fracture Parameters in Side-Grooved Compact Specimens, TIS Report 80CRD211, General Electric Company, Schenectady, NY, September 1980.

6. DeLorenzi, H. G., 3-D Elastic-Plastic Fracture Analysis with ADINA, Computers and Structures, Vol. 13, pp. 613-621, 1981.

7. Bass, B. R. and Bryson, J. W., Computational Methods for Combined Thermo-Mechanical Loading, Heavy Section Steel Technology Program Quarterly Progress Report for October-December 1981, NUREG/CR-2141/V4 (ORNL/TM-8252), Oak Ridge National Laboratory, Oak Ridge, TN, pp. 3-14, April 1982.

8. Moran, B., and Shih, C. F., Crack Tip and Associated Domain Integrals from Momentum and Energy Balance, Engineering Fracture Mechanics, Vol. 27, pp. 615-642, 1987.

APPENDIX B

TABLES AND FIGURES

Table 2.1. Stress-plastic-strain modulus H′ for HSST wide-plate material (HSST plate 13A of A533 grade B class 1 steel)

Plastic Strain Interval (%)	Temperature Interval (°C)	$H' = \Delta\sigma/\Delta\epsilon^{P}$ (MPa/%)
<1	$-125.00 < T < -72.78$	0.345
	$-72.78 \leq T < 37.78$	16.044 + 0.214 T
	$37.78 \leq T < 148.89$	21.787 + 0.062 T
	$148.89 \leq T < 260.00$	-24.407 + 0.372 T
1–2	$-125.00 < T < 260.00$	37.23
2–4	$-125.00 < T < 260.00$	26.579 - 0.00776 T
4–8	$-125.00 < T < 37.78$	11.228 - 0.0599 T
	$37.78 \leq T < 260.00$	8.96
8–12	$-125.00 < T < -17.78$	-0.0276 - 0.0403 T
	$-17.78 \leq T < 260.00$	0.689

Table 2.2 Fracture-toughness results for wide-plate specimen (WP-1) material (HSST plate 13A, A533 grade B class 1 steel)

Specimen	Test temperature (°C)	Thickness (mm)	a/w_i	Ductile Δa (mm)	J_{max} (kJ/m²)	J_{cleave} (kJ/m²)	K_{Jc} (MPa·√m)	$K_{Jcleave}$ (MPa·√m)	Beta-corrected $K_{Jcleave}$ (MPa·√m)
K33A	−150	50.8	0.554	<0.02	9.2	9.2	44.6	44.6	44.2
K33B	−150	50.8	0.555	<0.2	15.8	15.8	58.4	58.4	57.0
K34A	−75	50.8	0.556	0.071	97.5	97.5	143.6	143.6	102.7
K34B	−18	50.8	0.562	0.366	242.7	242.7	203.8[a]	224.8	119.9
K35A	−150	50.8	0.555	<0.02	10.2	10.1	46.7	46.7	46.2
K35B	−150	50.8	0.543	<0.02	7.5	7.5	40.2	40.2	40.0
K41B	−18	50.8	0.563	0.221	195.9	195.9	202.0	202.0	114.7
K42B	−75	50.8	0.563	<0.02	49.1	49.1	101.9	101.9	84.8
K51A	−18	25.4	0.573	1.049	501.1	501.1	NM[b]	321.9	110.4
K51C	−75	25.4	0.554	<0.02	14.4	14.4	55.2	55.2	50.7
K51D	−18	25.4	0.570	0.157	136.4	136.4	168.0	168.0	86.2
K52B	−75	25.4	0.576	<0.02	26.3	26.3	74.6	74.6	62.5
K53E	−18	25.4	0.562	0.196	177.6	177.6	192.3	192.3	91.5
K53F	−18	25.4	0.572	0.064	64.5	64.5	115.9	115.9	74.0
K54A	−75	25.4	0.573	<0.02	74.1	74.1	125.2	125.2	82.6
K54E	−18	25.4	0.567	0.069	83.1	83.1	131.1	131.1	77.7
K54F	−18	25.4	0.568	1.122	124.4	124.4	160.9	160.9	85.2

[a] J_{Ic} used to calculate K_{Jc}; otherwise J_{max} load used.

[b] NM = not measured.

Table 3.1. Summary of HSST wide-plate crack-arrest test conditions and results for A533 grade B class 1 steel: WP-1 series

Test No.	Crack location (cm)	Crack temperature (°C)	Initiation load (MN)	Arrest location (cm)	Arrest temperature (°C)	Arrest $T - RT_{NDT}$ (°C)	Crack-arrest toughness[e] (MPa·$\sqrt{m}$)
WP-1.1[a]	20.0	-60	20.10	50.2	51	74	NA
WP-1.2A	20.0	-33	18.90	55.5	62	85	424
WP-1.2B	55.5	62	18.90	64.5	92	115	685
WP-1.3	20.0[b]	-51	11.25	48.5	54	77	235
WP-1.4A	20.7[b,c]	-63	7.95	44.1	29	52	NA
WP-1.4B	44.1	29	9.72	52.7	60	83	387
WP-1.5A	20.0[b]	-30	11.03	52.1	56	79	231
WP-1.5B	52.1	56	11.03	58.0	72	95	509
WP-1.6A	20.0[b]	-19	14.50	49.3	54	77	275
WP-1.6B	49.3	54	14.50	59.3	80	103	397
WP-1.7A	20.2[b]	-24	26.20	52.8	61	84	319
WP-1.7B	52.8	61	26.20	63.5	88	111	555
WP-1.8A	19.8[b]	-47	26.50	44.9	40	63	345
WP-1.8B	44.9	40	26.50	50.4	55	78	484
WP-1.8C	50.4	55	26.50	59.4	79	102	563

[a]Specimen was warm prestressed by loading to 10 MN at 70°C. Specimen was also preloaded to 19 MN.
[b]Crack front cut to truncated chevron configuration.
[c]Pillow jack utilized to apply pressure load to specimen's machined notch.
[d]Specimen was warm prestressed to 14 MN at 25°C.
[e]Dynamic finite element analyses

Table 3.2. Initiation stress-intensity factor comparisons for the WP-1 series of wide-plate crack arrest tests

Test designation	Crack-tip temperature (°C)	Calculated static K_I (MPa·$\sqrt{m}$)	Property correlation K_{Ic}[c] (MPa·$\sqrt{m}$)	K_I/K_{Ic}
WP-1.2	-33.0	251.5[a]	87.5	2.87
WP-1.3	-51.0	173.5[b]	70.1	2.48
WP-1.4	-62.0	213.0[b]	63.9	3.33
WP-1.5	-30.0	179.8[b]	91.6	1.96
WP-1.6	-19.0	233.8[b]	111.2	2.10
WP-1.7	-22.7	280.6[b]	103.7	2.71
WP-1.8	-47.2	290.0[b]	73.0	3.97

[a]Computed from 2-D static analysis.
[b]Computed from 3-D static analysis.
[c]Calculated from $K_{Ic} = 51.276 + 51.897e^{0.036(T-RT_{NDT})}$ using crack-tip temperature of initial flaw and material RT_{NDT}.

Table 5.1. Comparison of CT and WP specimens at $r/\delta_t = 4$

Spec	J (MJ/m²)	r (mm)	δ_t (mm)	σ_{p1} (MPa)	J_{SSY} (MJ/m²)	J/J_{SSY}
2T-CT[a]	.0480	.273	.0682	1402	.0240	2.0
	.0586	.327	.0818	1410	.0294	2.0
	.0615	.342	.0854	1417	.0315	2.0
	.0775	.421	.1053	1420	.0392	2.0
2T-CT[b]	.1075	.604	.1511	1337	.0560	1.9
	.1149	.637	.1592	1331	.0577	2.0
1T-CT[c]	.0173	.120	.0301	1427	.0115	1.5
	.0199	.137	.0342	1412	.0125	1.6
	.0262	.174	.0435	1386	.0145	1.8
	.0845	.480	.1225	1376	.0385	2.2
WP[d]	.0517	.218	.0545	1315	.0142	3.6
	.0600	.248	.0620	1327	.0168	3.6
	.0691	.280	.0699	1333	.0193	3.6
	.0788	.313	.0783	1338	.0220	3.6
	.2457	.850	.2125	1348	.0618	4.0
WP[e]	.0512	.225	.0563	1256	.0142	3.6
	.0595	.256	.0641	1263	.0166	3.6
	.0685	.289	.0724	1268	.0191	3.6
	.0780	.324	.0810	1274	.0218	3.6
	.2440	.894	.2235	1266	.0585	4.2
WP[f]	.0895	.463	.1157	1441	.0575	1.6
	.1463	.749	.1873	1398	.0800	1.8
	.2545	1.270	.3164	1378	.1250	2.0

[a] 2-D elastic-plastic static analysis at T = -75°C.
[b] 2-D elastic-plastic static analysis at T = -18°C.
[c] 3-D elastic-plastic static analysis at T = -75°C.
[d] 2-D elastic-plastic static analysis at T = -75°C.
[e] 2-D elastic-plastic static analysis at T = -33°C.
[f] 3-D thermo-elastic-plastic static analysis with thermal gradient and T_{CT} = -33°C.

Table 5.2. Cumulative area within the maximum principal stress contour σ_{p1} = 1400 MPa for CT and WP specimens

Spec	Load (MN)	J (MJ/m^2)	Area (mm^2)	Normalized Area $A*(\sigma_o/J)^2$
2T-CT[a]	.144	.0480	.0658	6.7
	.158	.0586	.1083	7:4
	.162	.0615	.1139	7.0
	.180	.0775	.1786	7.0
2T-CT[b]	.203	.1075	.1387	2.2
	.207	.1149	.1501	2.2
1T-CT[c]	.029	.0173	.0060	4.7
	.031	.0199	.0060	3.5
	.035	.0262	.0163	5.6
	.050	.0845	.1272	4.2
WP[d]	8.81	.0517	.0169	1.5
	9.48	.0600	.0253	1.6
	10.16	.0691	.0311	1.5
	10.84	.0788	.0650	2.5
	18.90	.2457	.3067	1.2
WP[e]	8.81	.0512	.0101	0.8
	9.48	.0595	.0106	0.6
	10.16	.0685	.0169	0.7
	10.84	.0780	.0253	0.9
	18.90	.2440	.1226	0.4
WP[f]	5.34	.0203	.0487	24.2
	11.49	.0895	.1976	5.1
	18.90	.2545	.4401	1.4

[a] 2-D elastic-plastic static analysis at T = -75°C.
[b] 2-D elastic-plastic static analysis at T = -18°C.
[c] 3-D elastic-plastic static analysis at T = -75°C.
[d] 2-D elastic-plastic static analysis at T = -75°C.
[e] 2-D elastic-plastic static analysis at T = -33°C.
[f] 3-D thermo-elastic-plastic static analysis with thermal gradient at T_{CT} = -33°C.

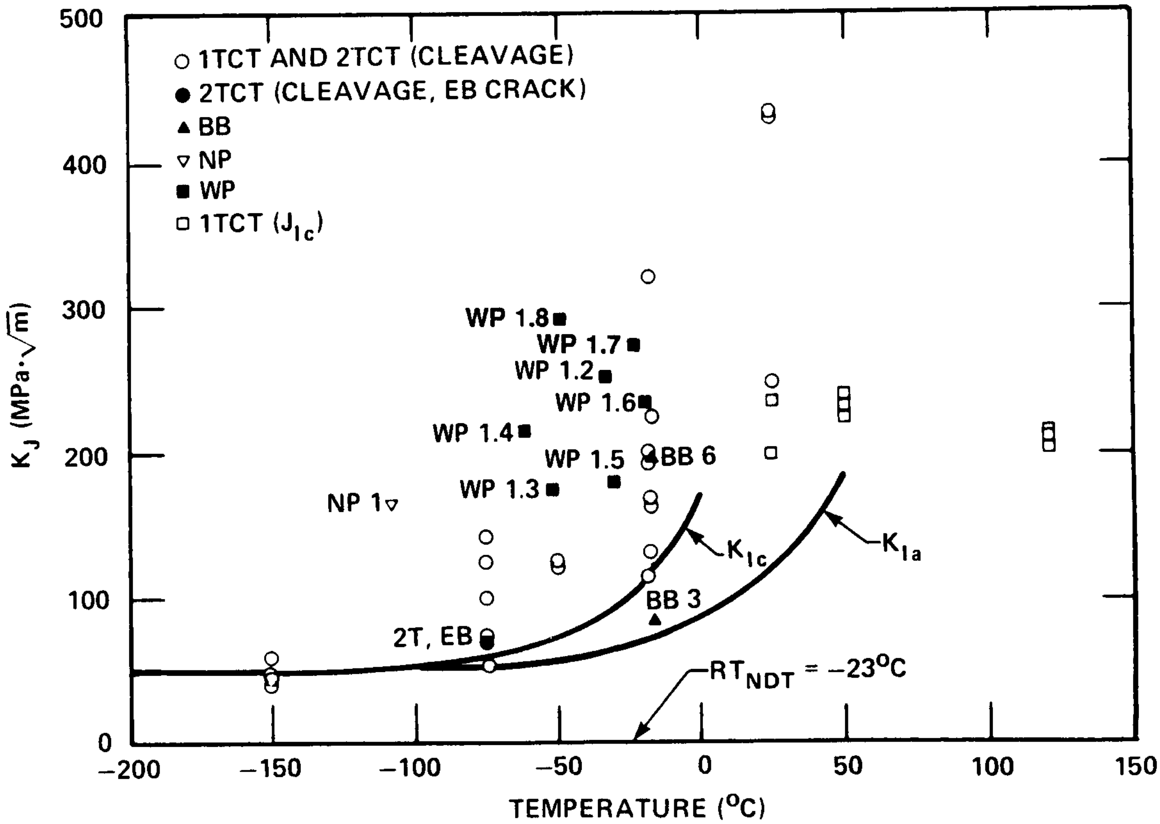

Figure 1.1. Cleavage initiation values vs. temperatures for small and large specimen tests of A533 grade B class 1 steel.

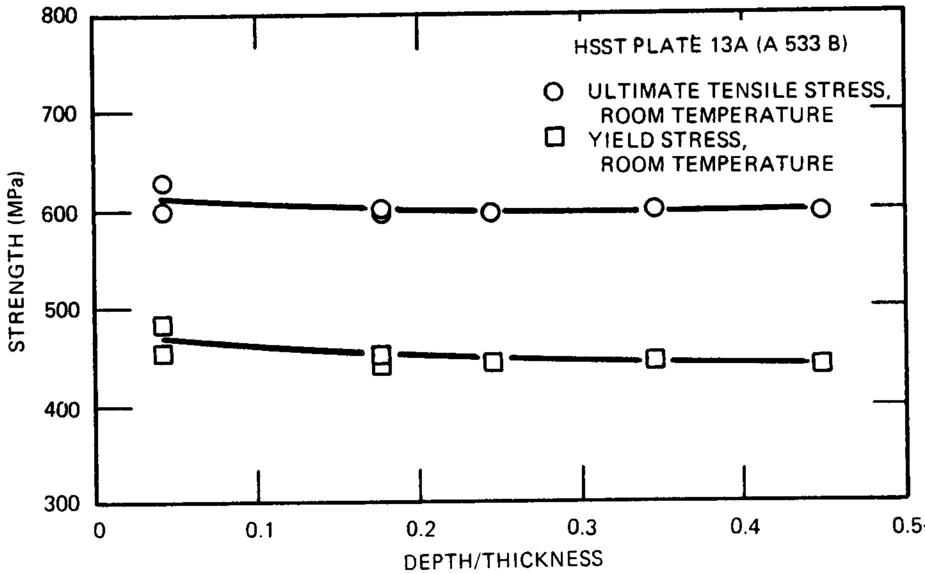

Figure 2.1. Longitudinal tensile properties through 18.7-cm thickness of HSST plate 13A, A533 grade B class 1 steel at room temperature.

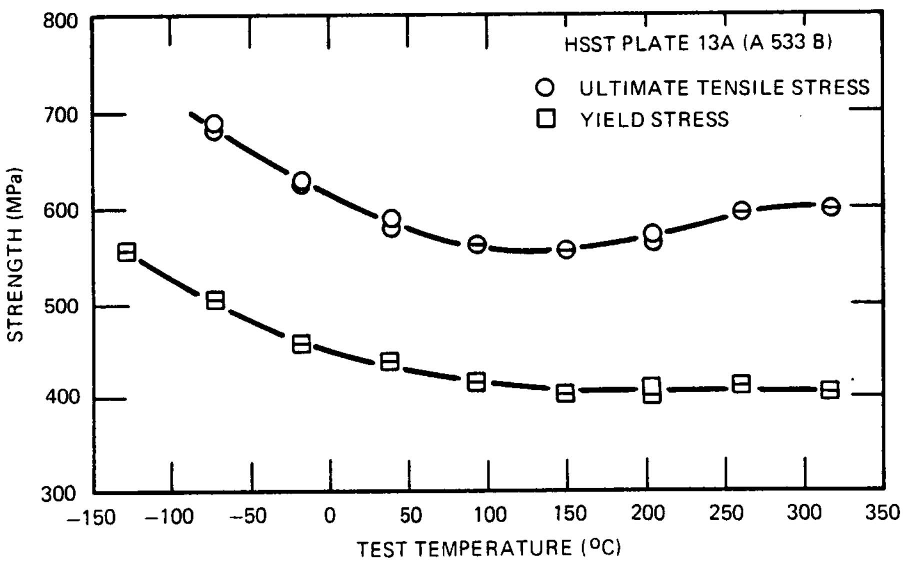

Figure 2.2. Effect of temperature on longitudinal tensile properties for HSST plate 13A, A533 grade B class 1 steel (specimens from center half of 18.7-cm-thick plate).

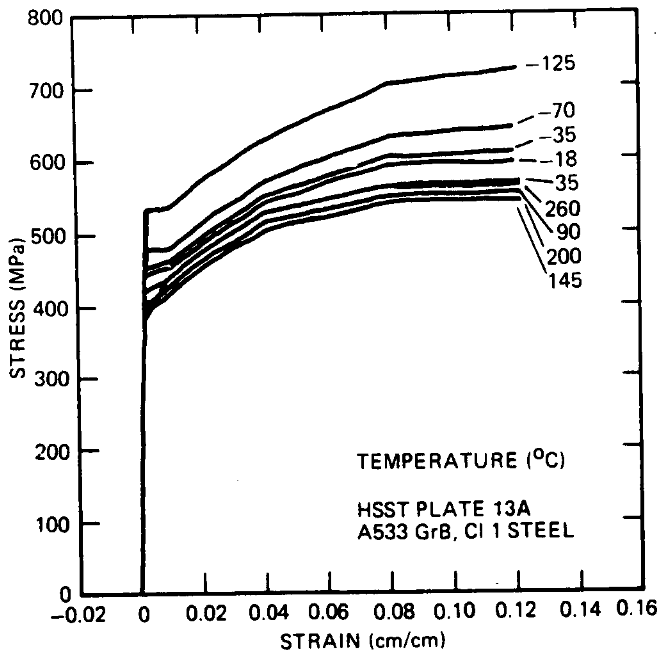

Figure 2.3. Multilinear representations of uniaxial stress-strain behavior of HSST plate 13A of A533 grade B class 1 steel.

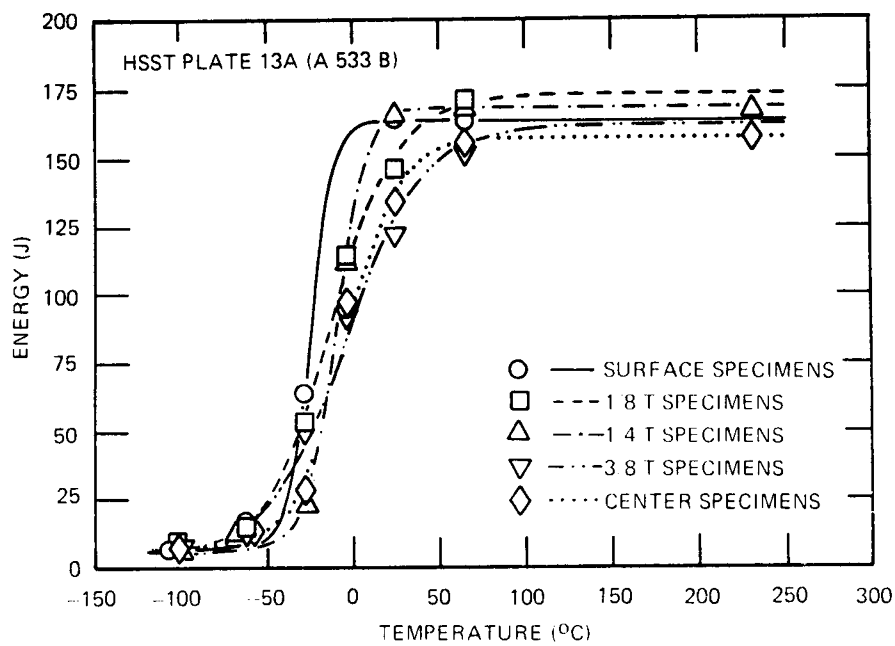

Figure 2.4. CVN through-thickness results for LT specimens from HSST plate 13A, A533 grade B class 1 steel in quenched and tempered condition.

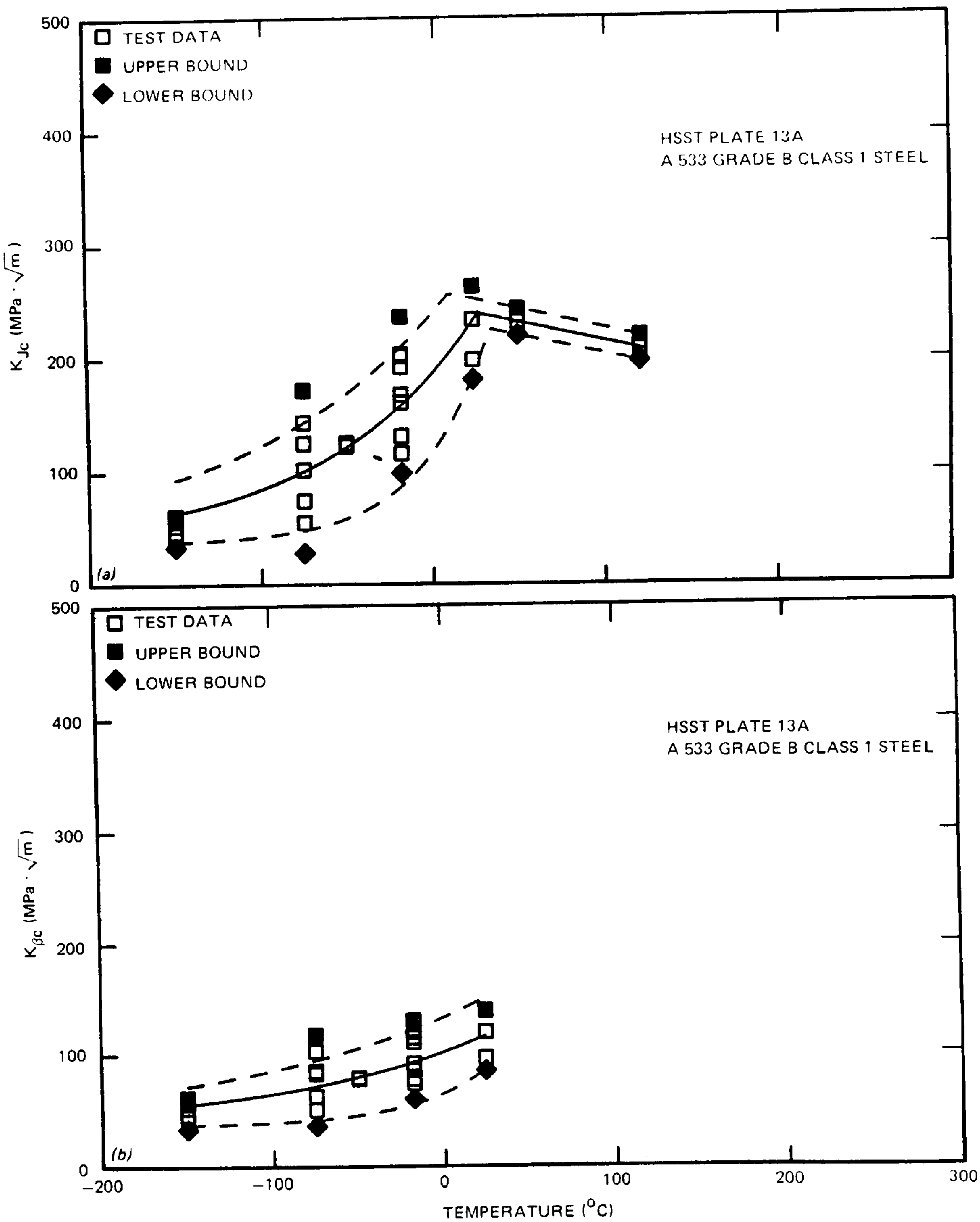

Figure 2.5. (a) Fracture toughness for HSST plate 13A showing upper and lower bounds and (b) beta-corrected fracture toughness for HSST plate 13A showing upper and lower bounds (two standard deviations from the mean).

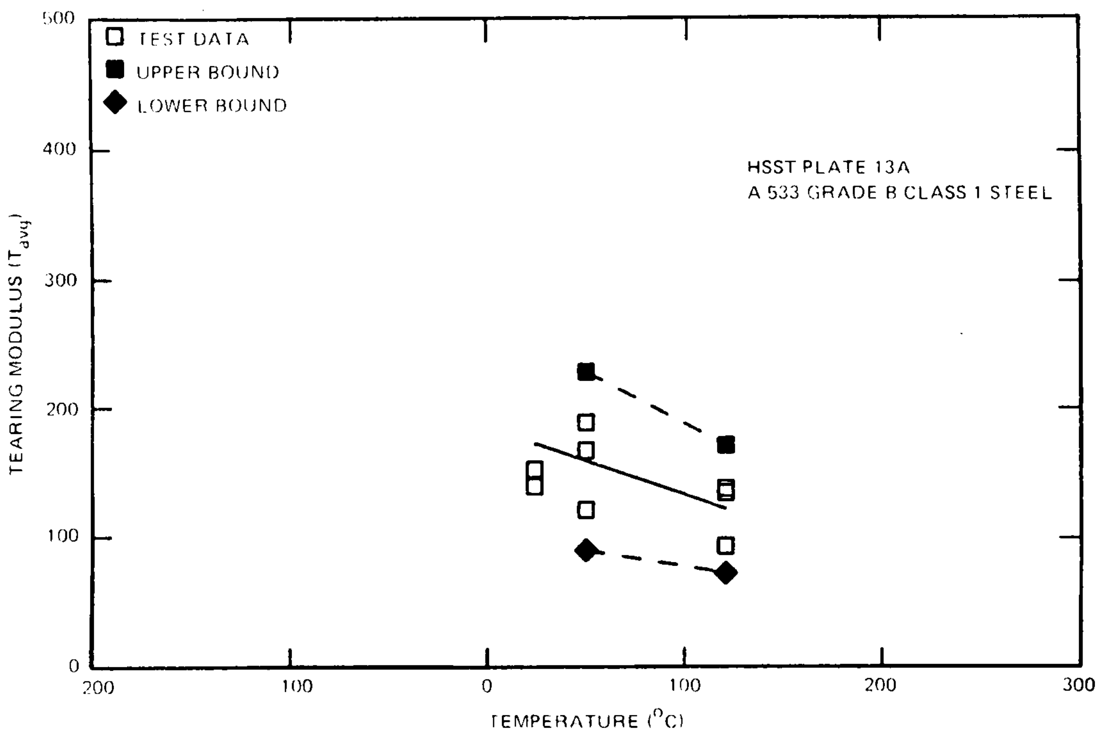

Figure 2.6. Tearing modulus for HSST plate 13A showing upper and lower bounds (two standard deviations from the mean).

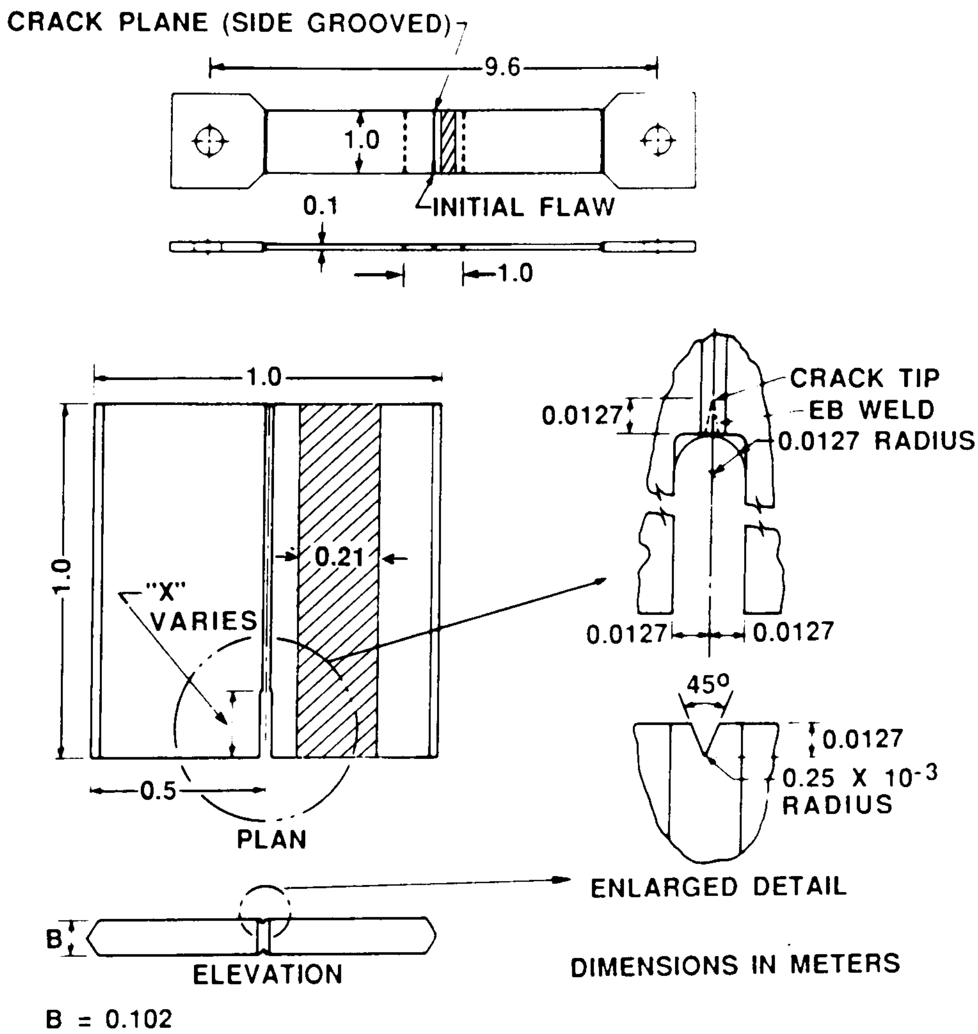

Figure 3.1. Schematic of HSST wide-plate crack-arrest specimen.

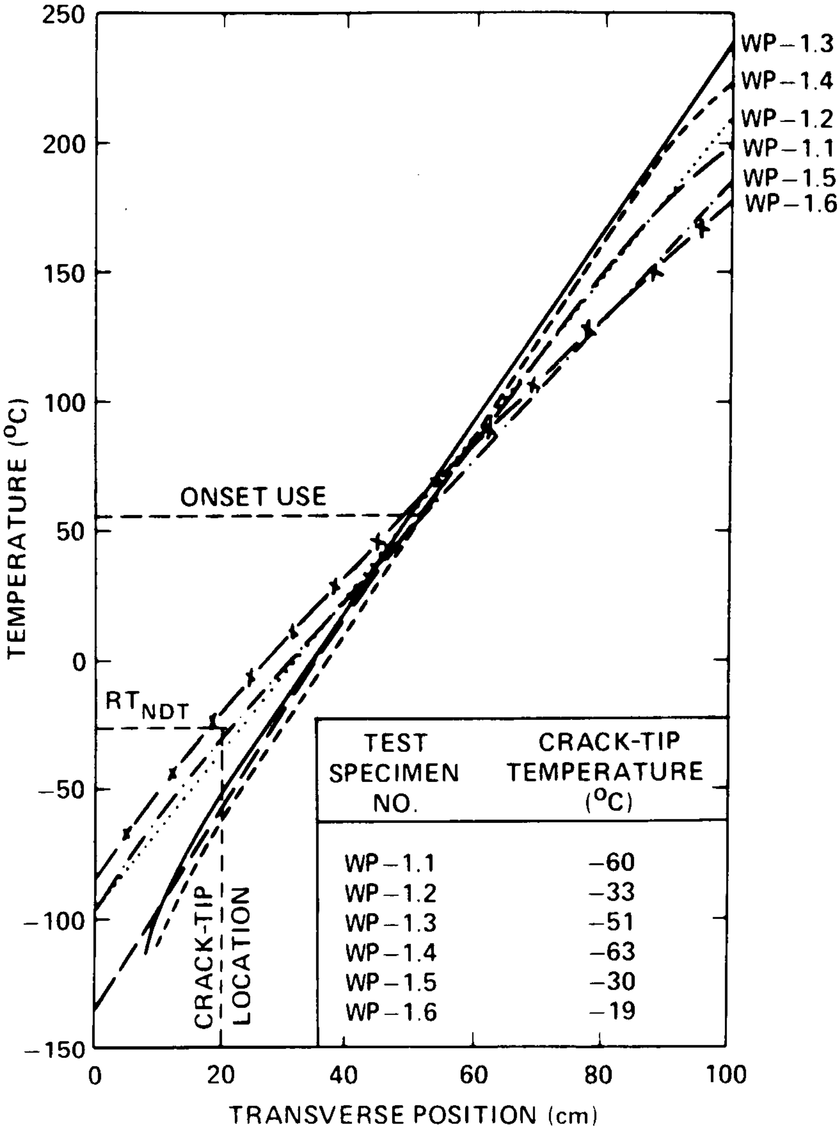

Figure 3.2. Transverse temperature profiles at approximate time of crack initiation-arrest events: Tests WP-1.1 through WP-1.6.

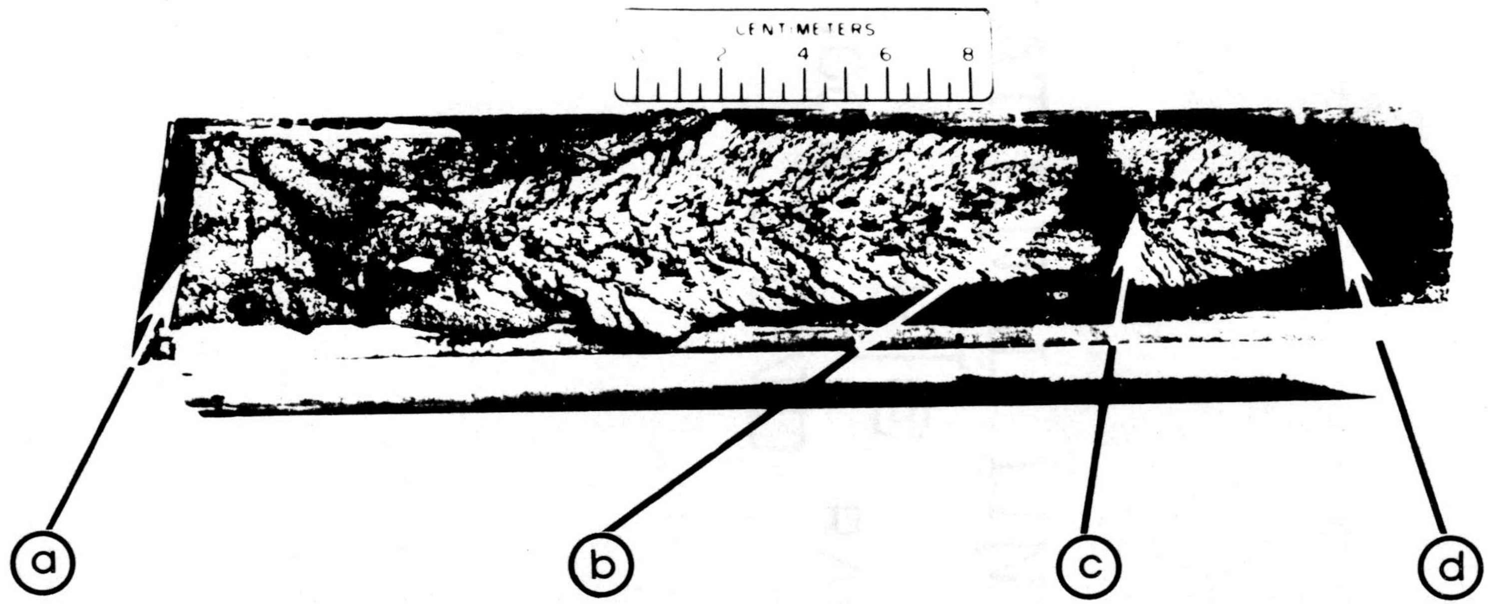

Figure 3.3. Portion of fracture surface indicating initiation and arrest events and associated temperatures for Test WP-1.2: (a) cleavage initiation; (b) first cleavage arrest and onset of ductile tearing; (c) second cleavage initiation; (d) second cleavage arrest and onset of unstable ductile tearing.

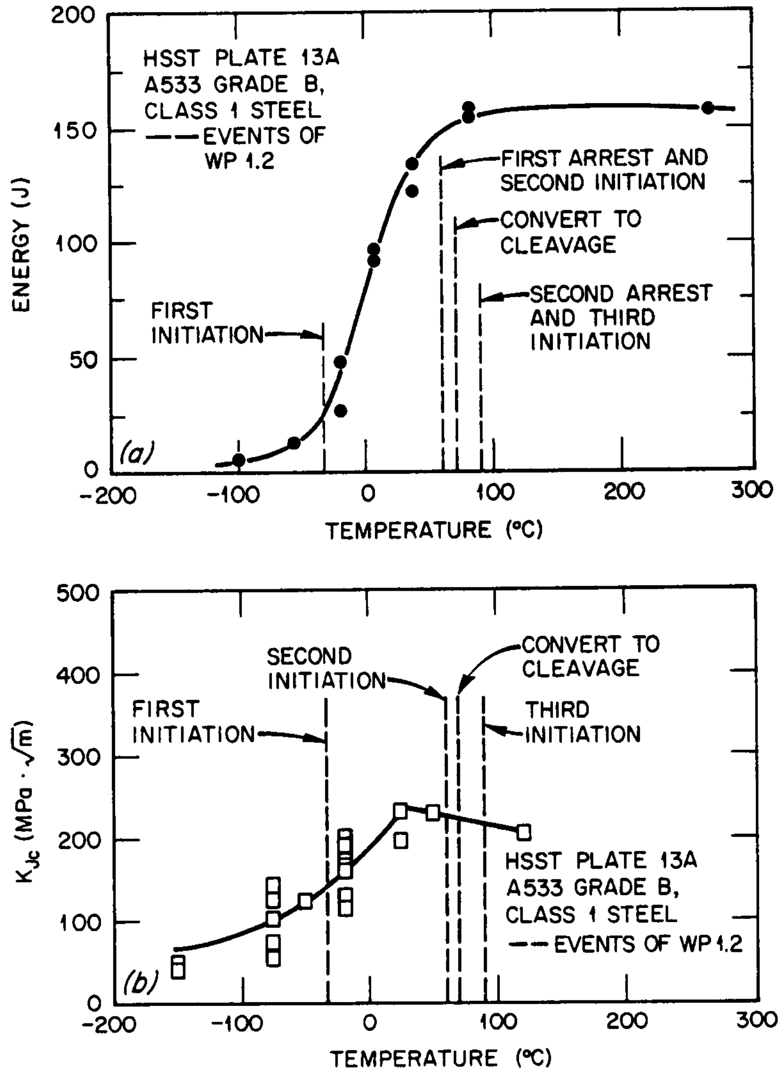

Figure 3.4. (a) Charpy V-notch impact and (b) fracture-toughness K_{Jc} curves for wide-plate series 1 material, HSST Plate 13A. Crack initiation and arrest events for WP-1.2 are superimposed on curves.

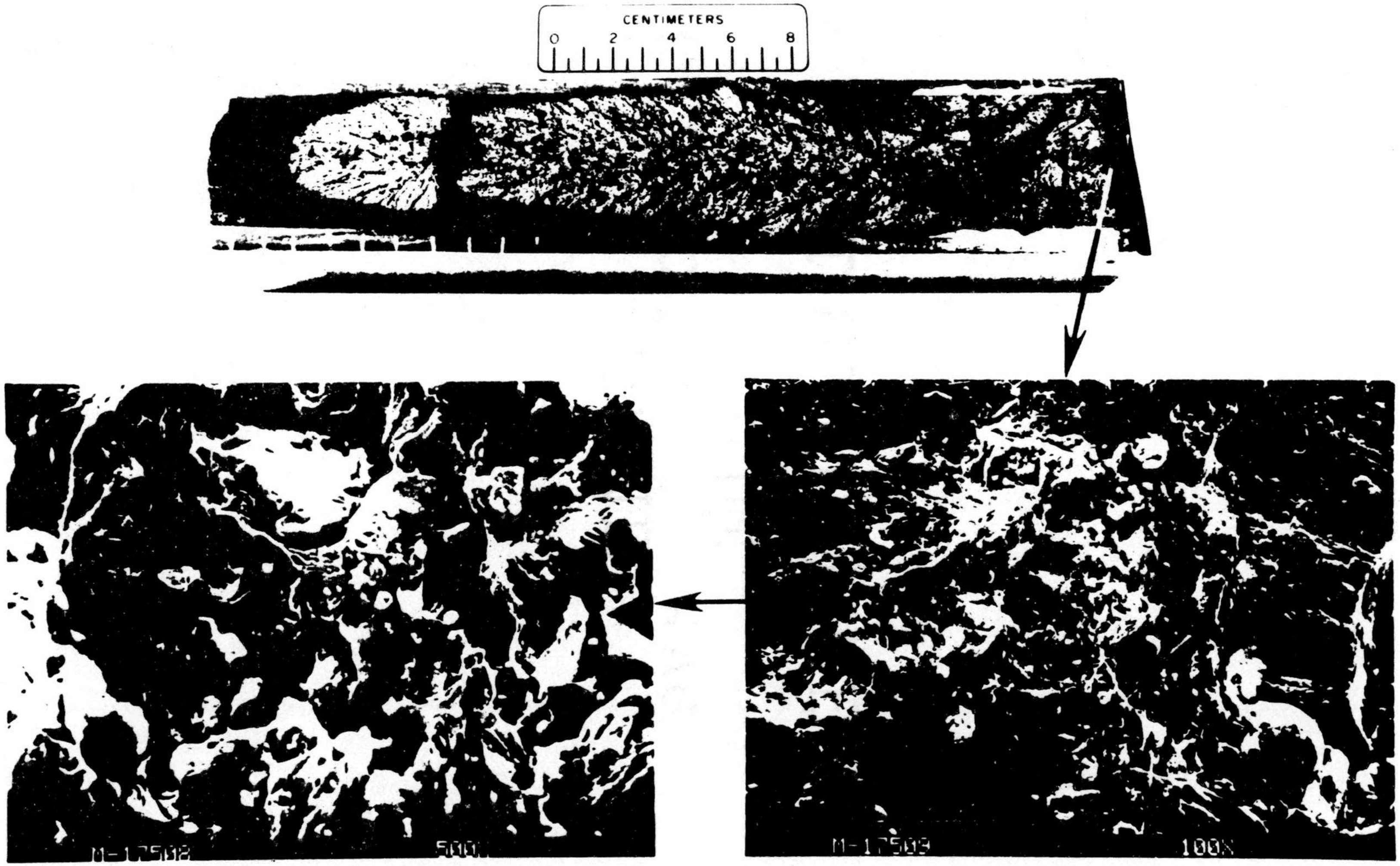

Figure 3.5. Scanning electron fractographs revealing no evidence of significant ductile tearing at first crack initiation event: Test WP-1.2.

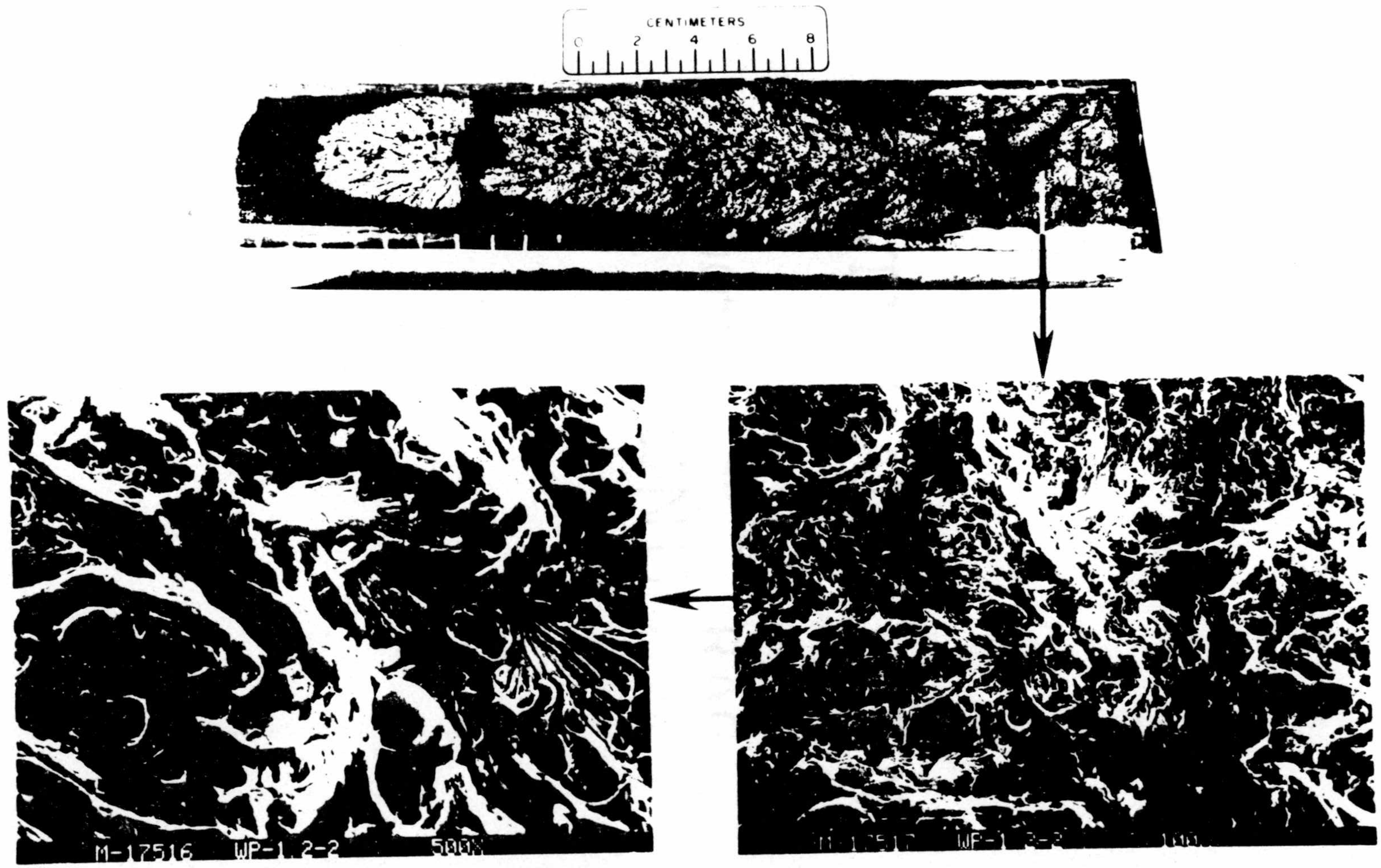

Figure 3.6. Scanning electron fractographs showing dominant mode of fracture to be cleavage during first crack run event: Test WP-1.2.

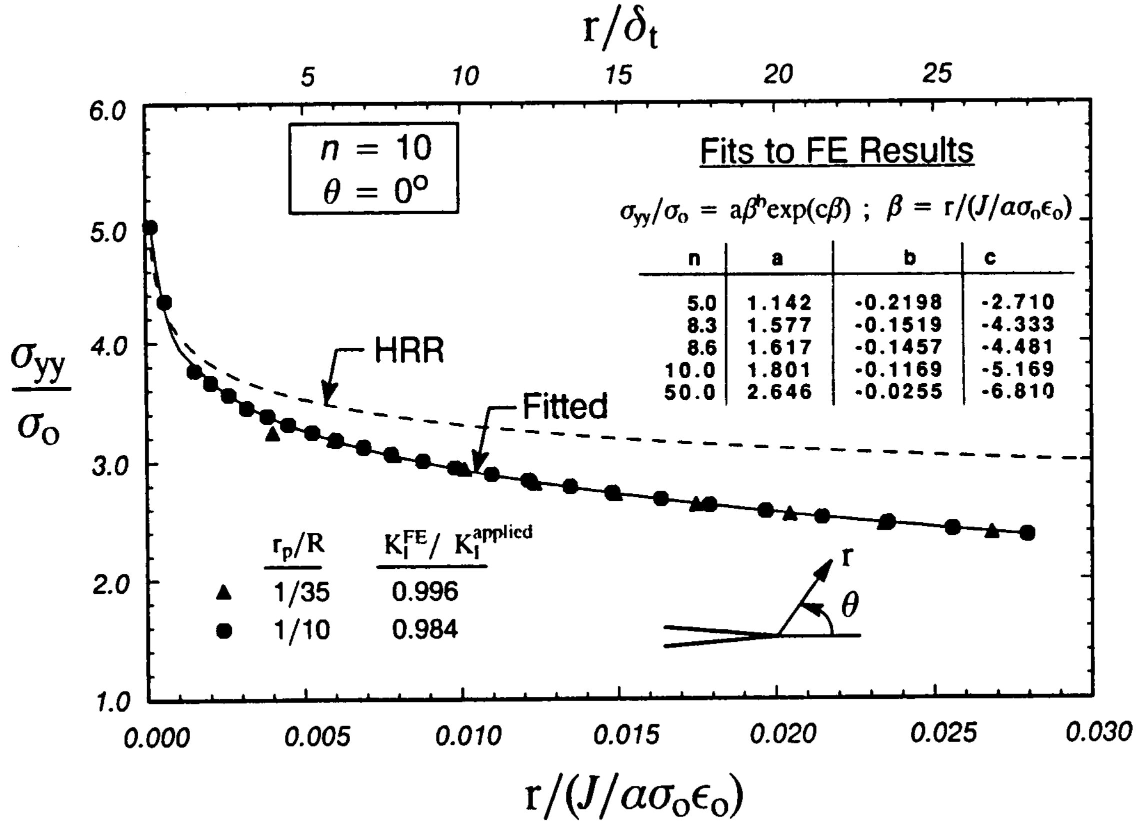

Figure 4.1. Comparison of normalized crack-opening stress in plane strain small-scale yielding and HRR solutions for hardening exponent n = 10 at two levels of loading. Table of curve-fitting parameters for small-scale yielding response for various hardening exponents are superposed.

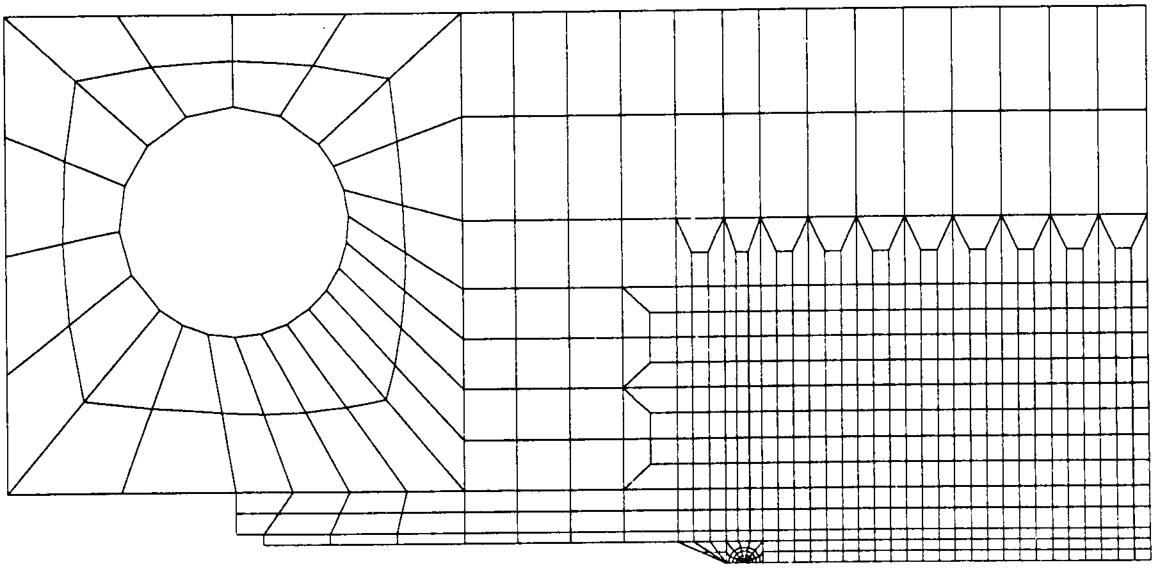

Figure 5.1. Two-dimensional finite element model for the 2T-CT specimen.

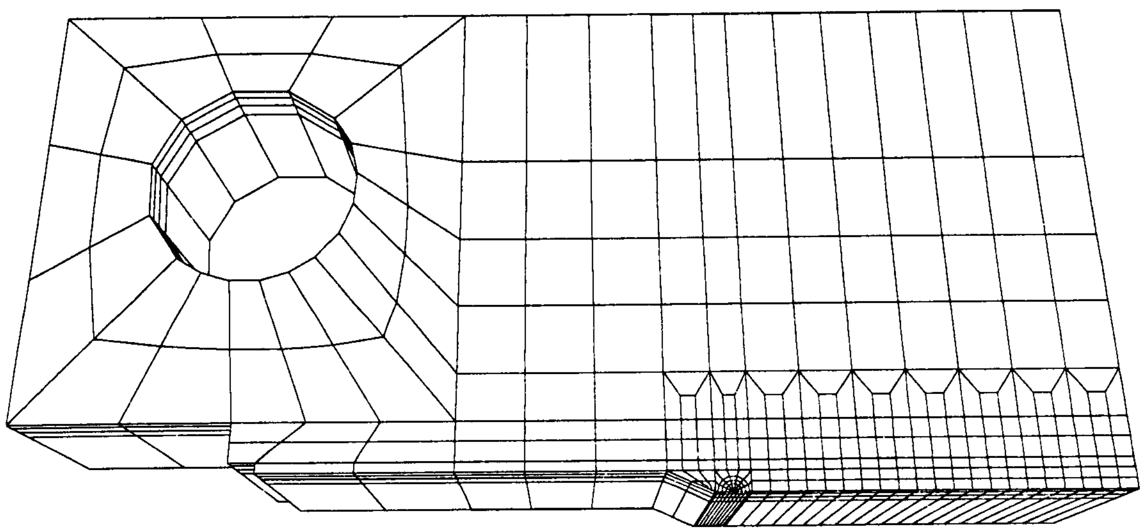

Figure 5.2. Three-dimensional finite element model for the 2T-CT specimen.

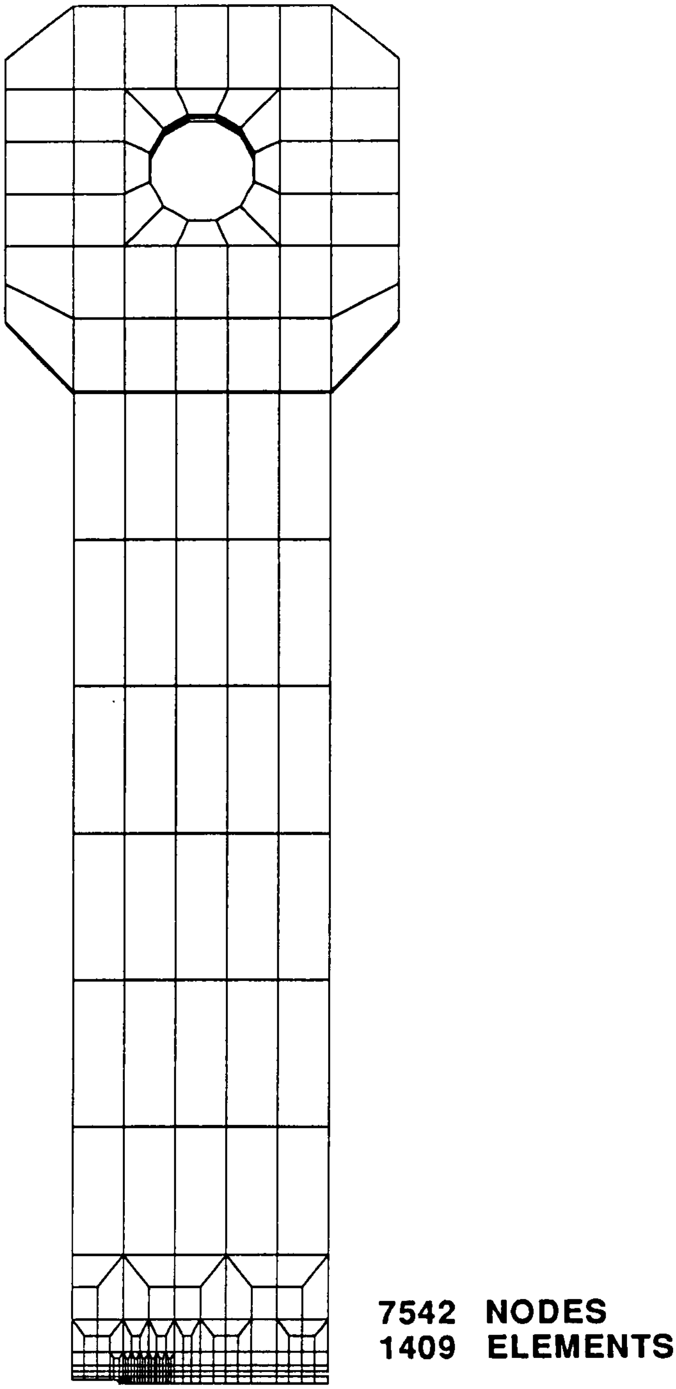

Figure 5.3. Three-dimensional finite element model for the WP specimen.

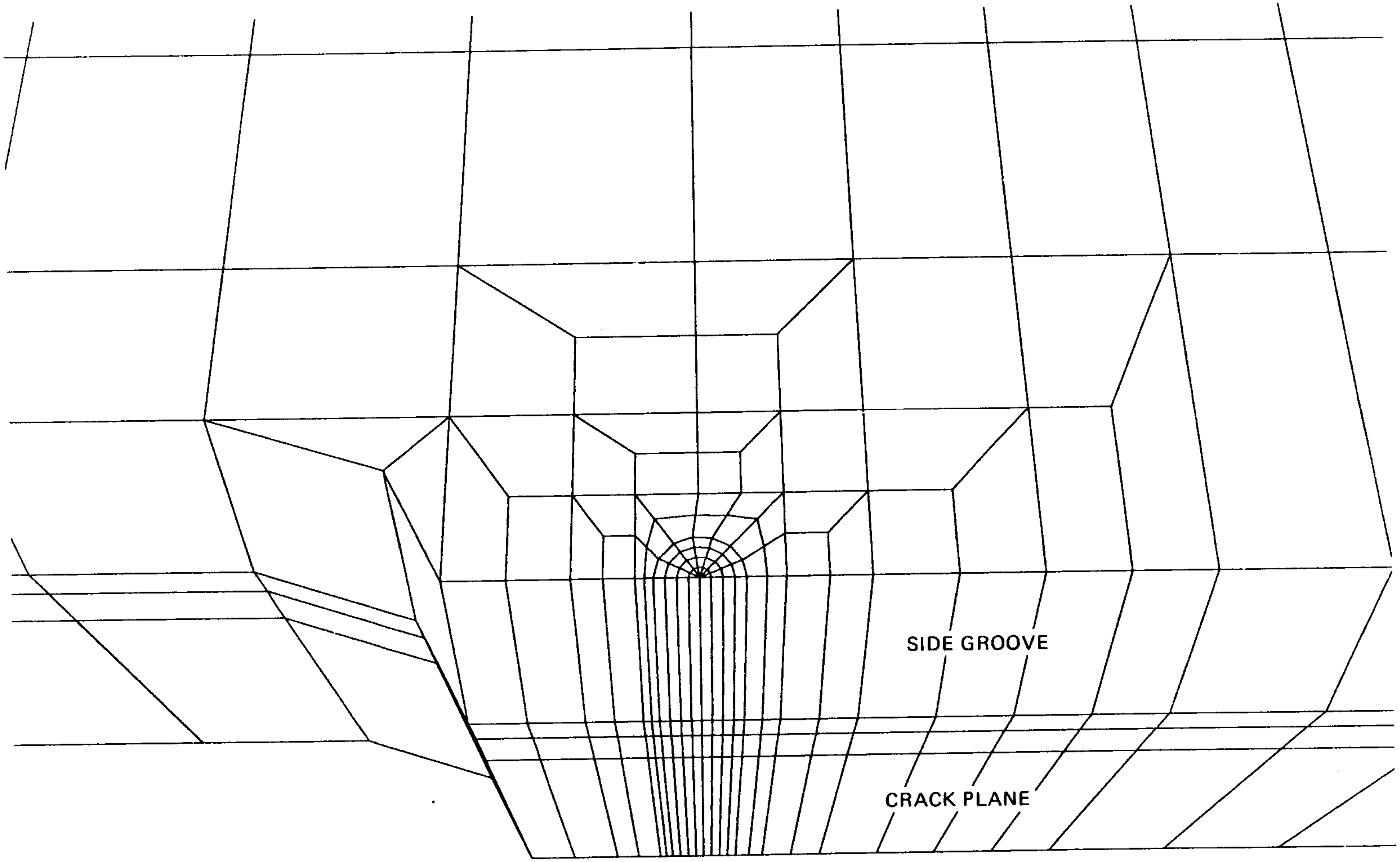

Figure 5.4. Crack-tip region of the 3-D finite element model for the WP specimen.

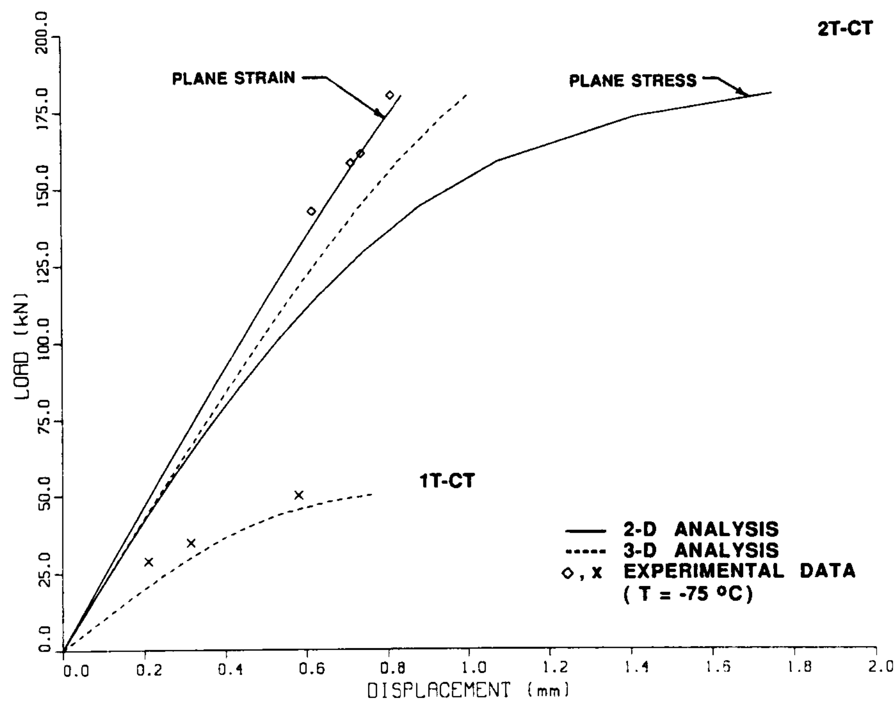

Figure 5.5. Results of elastic-plastic analyses for the CT specimens at -75°C showing load vs. crack-mouth opening displacement (CMOD).

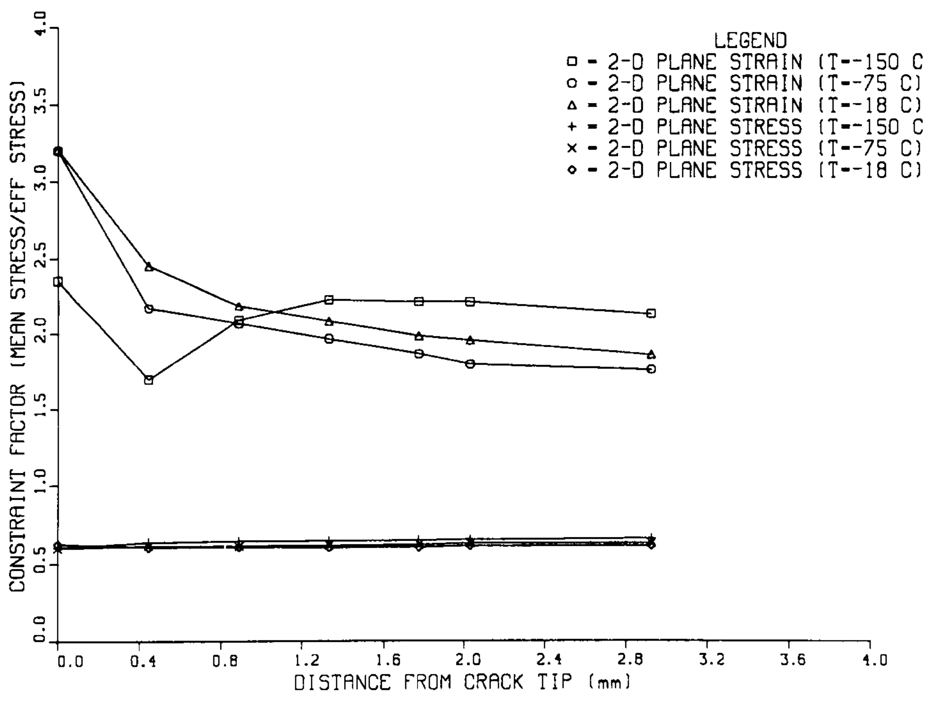

Figure 5.6. Comparison of the plane stress and plane strain 2-D elastic-plastic analyses for the 2T-CT specimen at -150°C, -75°C, and -18°C.

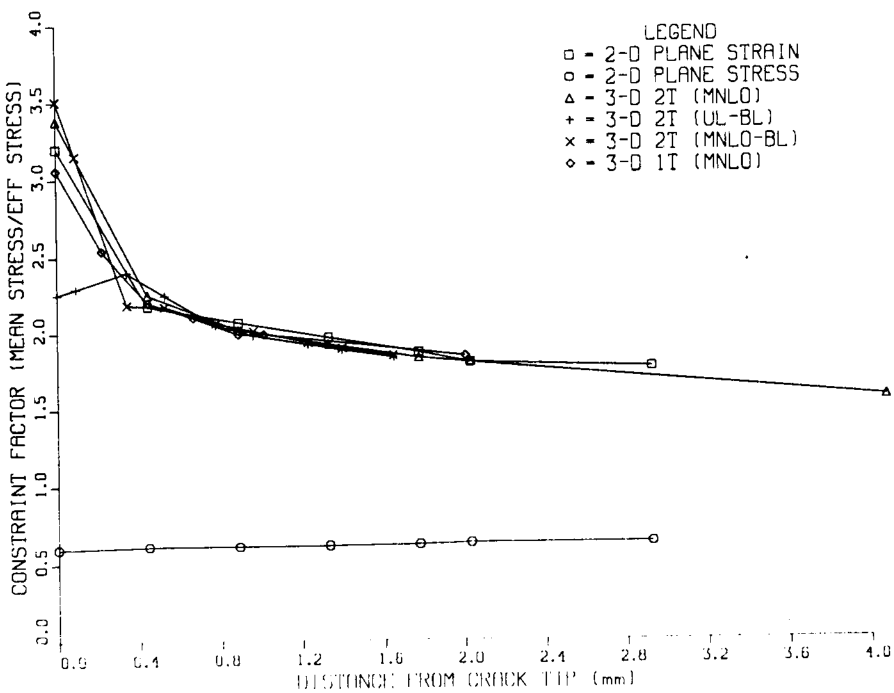

Figure 5.7. Constraint vs. distance from the crack tip from elastic-plastic analyses for the 1T- and 2T-CT specimens at -75°C.

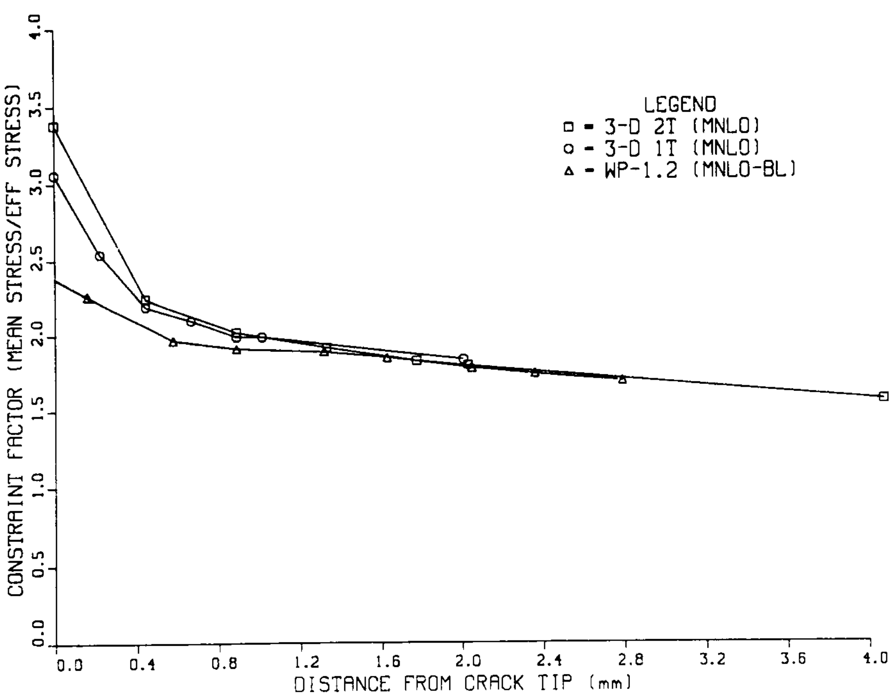

Figure 5.8. Constraint vs. distance from the crack tip from 3-D elastic-plastic analyses for the CT specimens at -75°C and the WP specimen at -33°C.

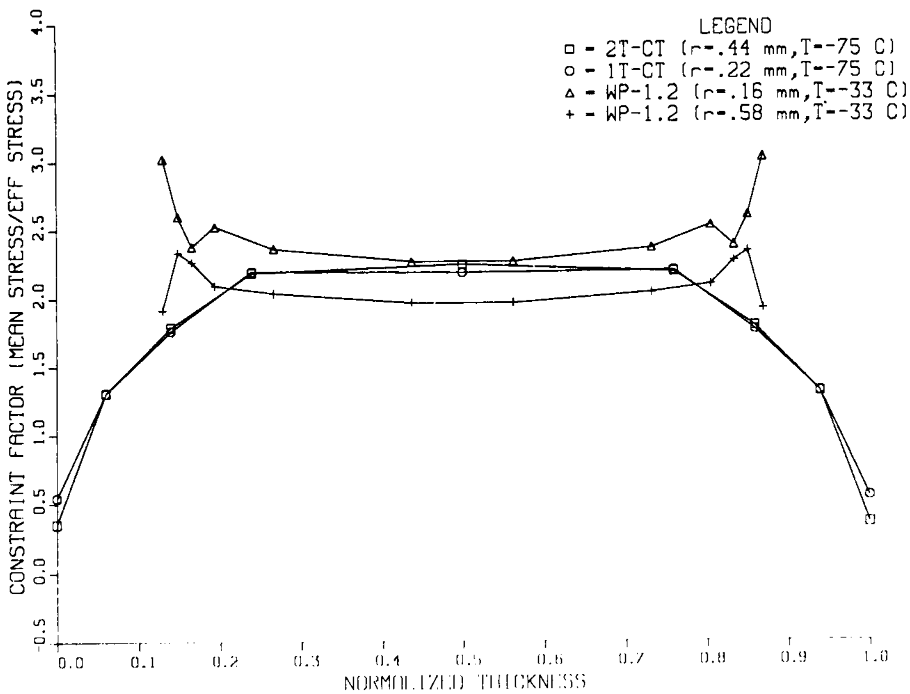

Figure 5.9. Comparison of the thru-thickness constraint for the CT and WP specimens from 3-D elastic-plastic analyses.

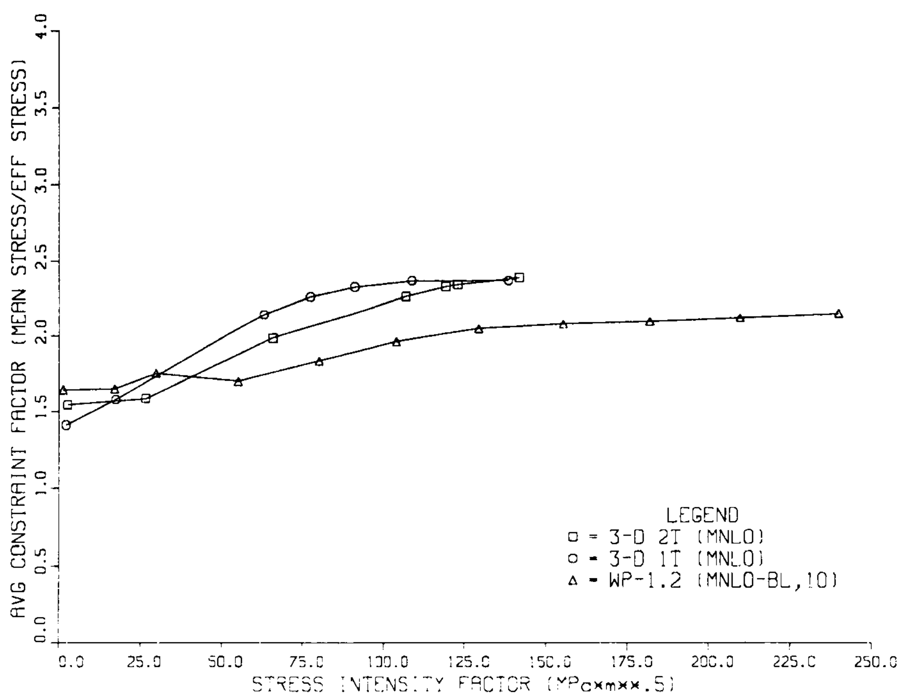

Figure 5.10. Comparison of the thru-thickness average constraint for increasing load for the CT specimens at -75°C and the WP specimen at -33°C from 3-D elastic-plastic analyses.

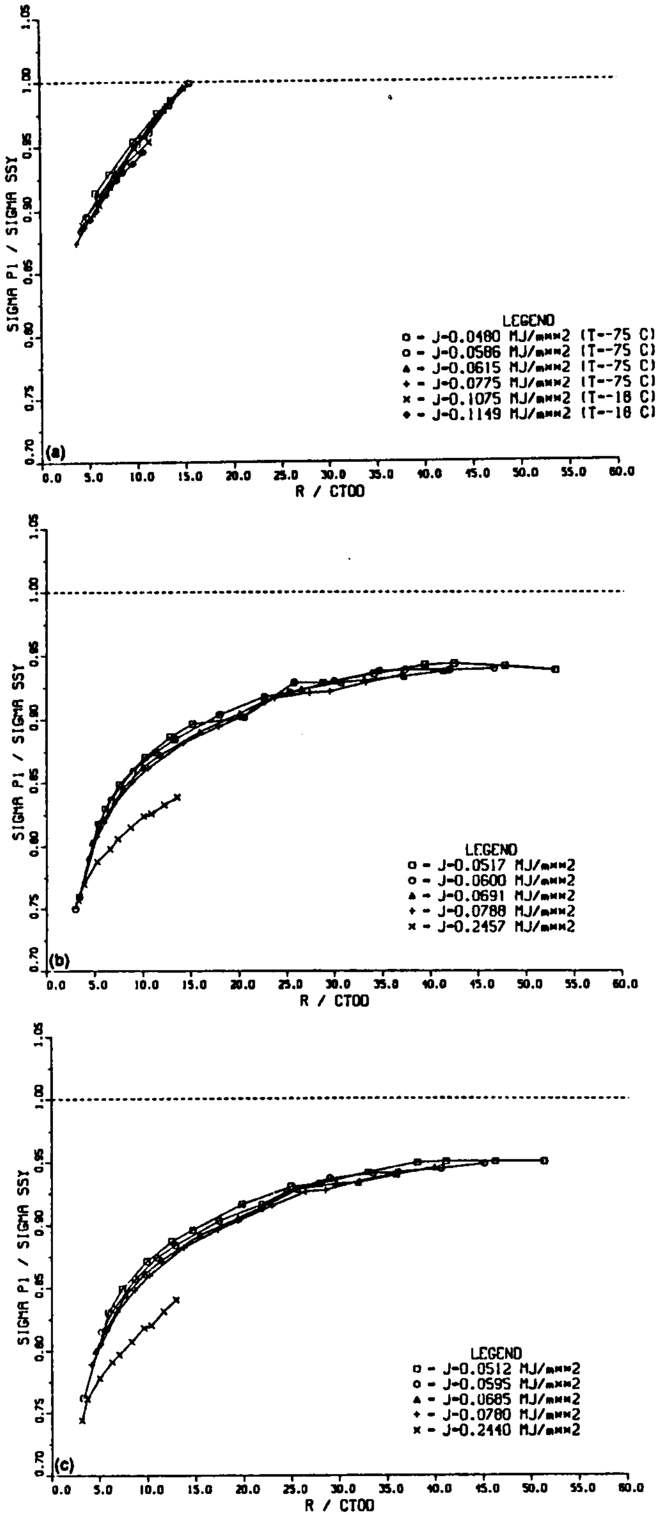

Figure 5.11. Normalized crack-opening stress vs. normalized distance ahead of the crack tip: (a) 2T-CT specimens at -75°C and -18°C; (b) WP specimen at -75°C; (c) WP specimen at -33°C.

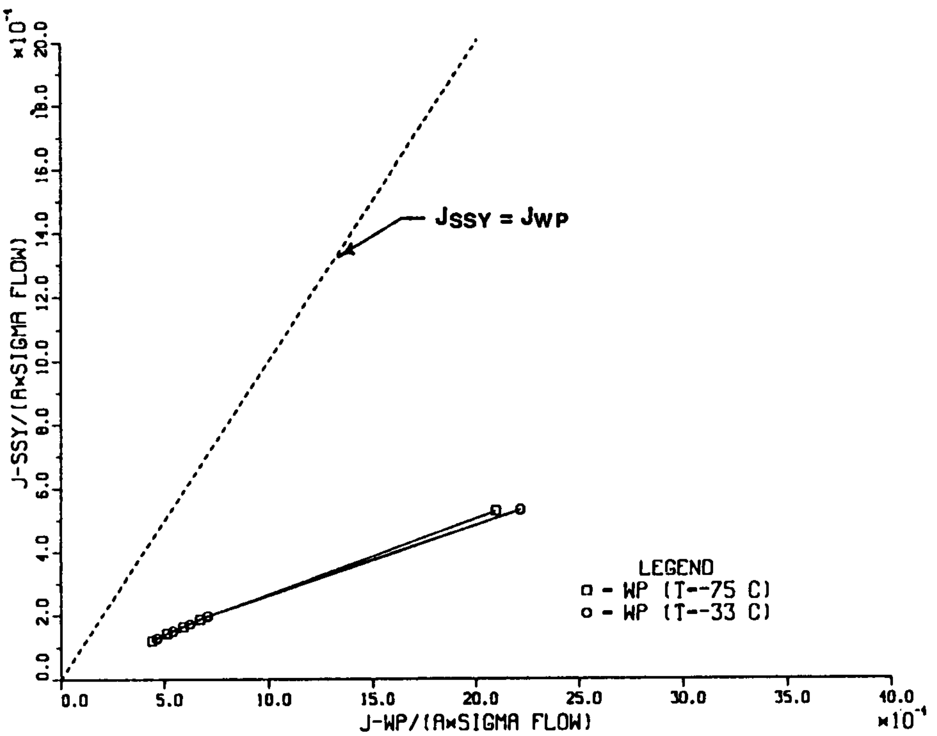

Figure 5.12. Normalized J-integral values vs. those at SSY conditions which generate equivalent opening-mode stresses ahead of the crack tip in the WP specimen at -75°C and -33°C.

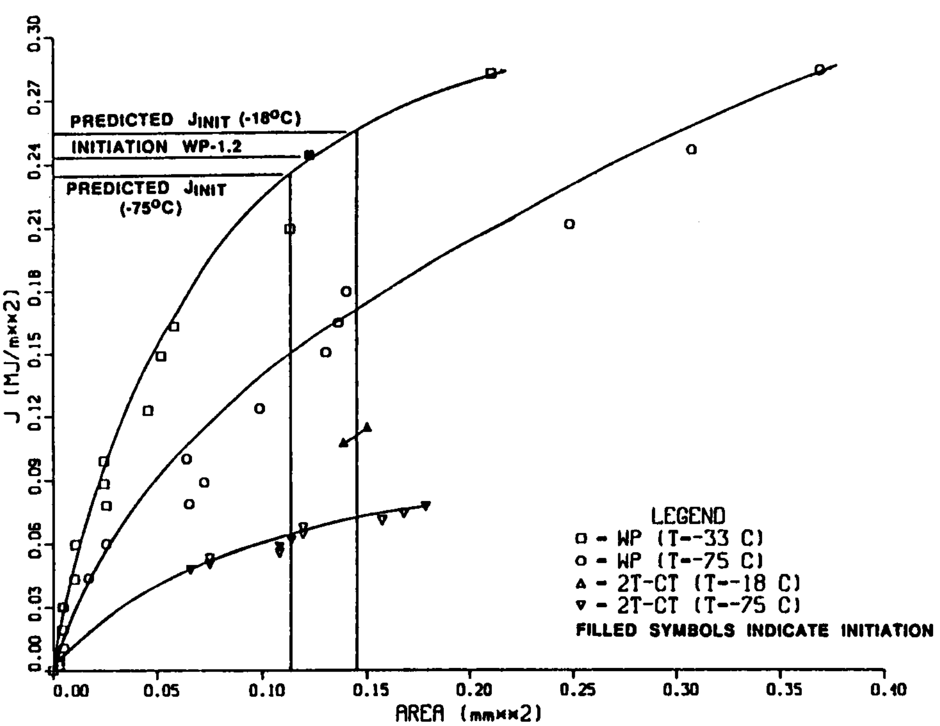

Figure 5.13. J-integral values vs. cumulative area within a critical stress contour of 1400 MPa in the 2T-CT and WP specimens.

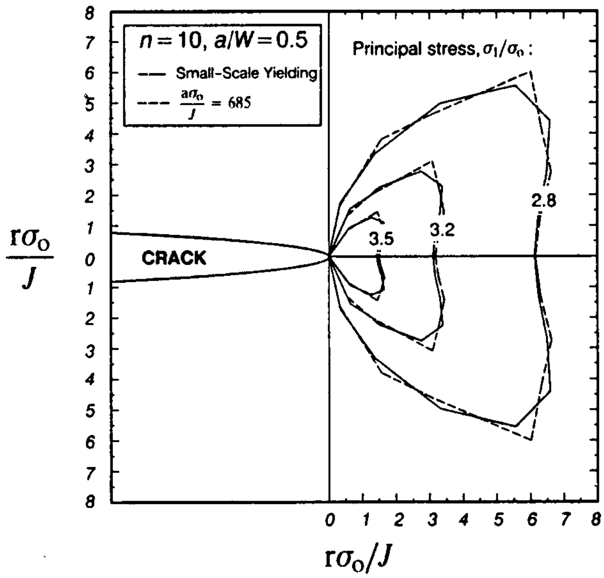

Figure 5.14. Comparison of principal stress contours in small-scale yielding and in a SENB specimen for a/W = 0.5 and hardening exponent of n = 10 (from Ref. [17]).

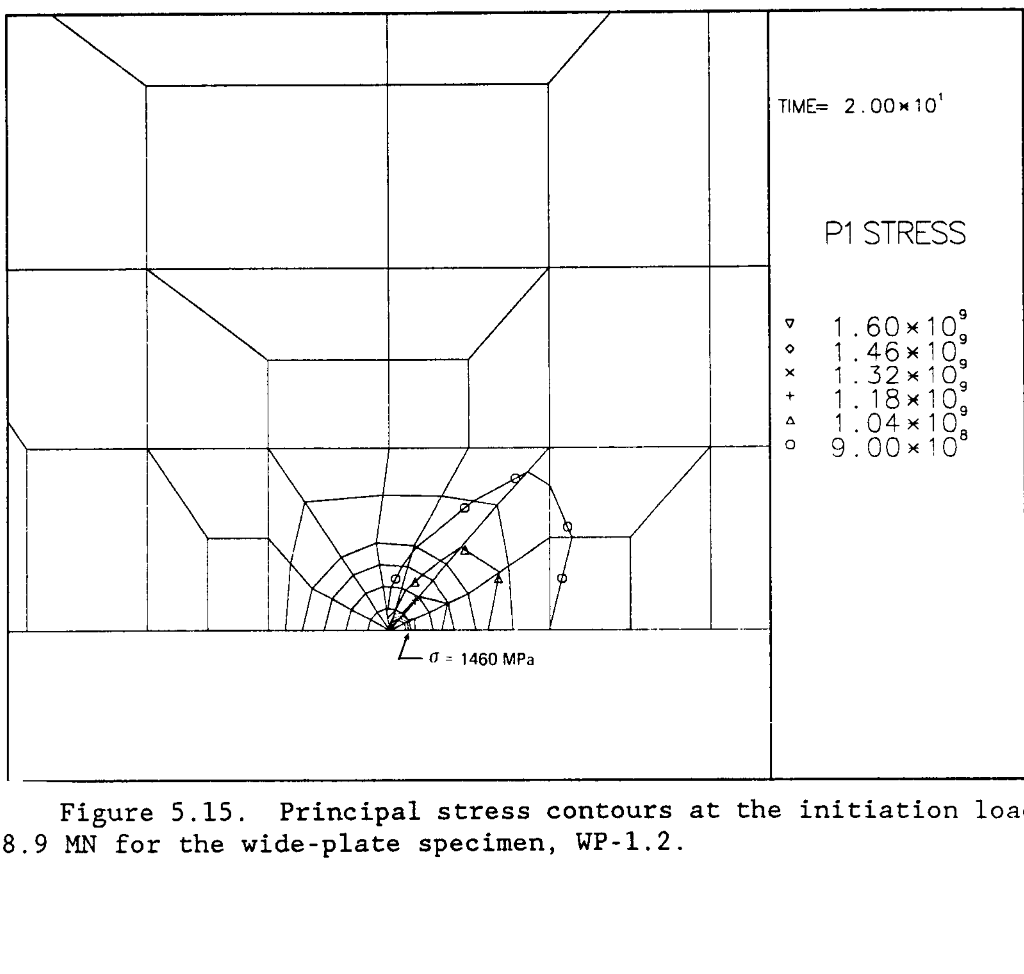

Figure 5.15. Principal stress contours at the initiation load of 18.9 MN for the wide-plate specimen, WP-1.2.

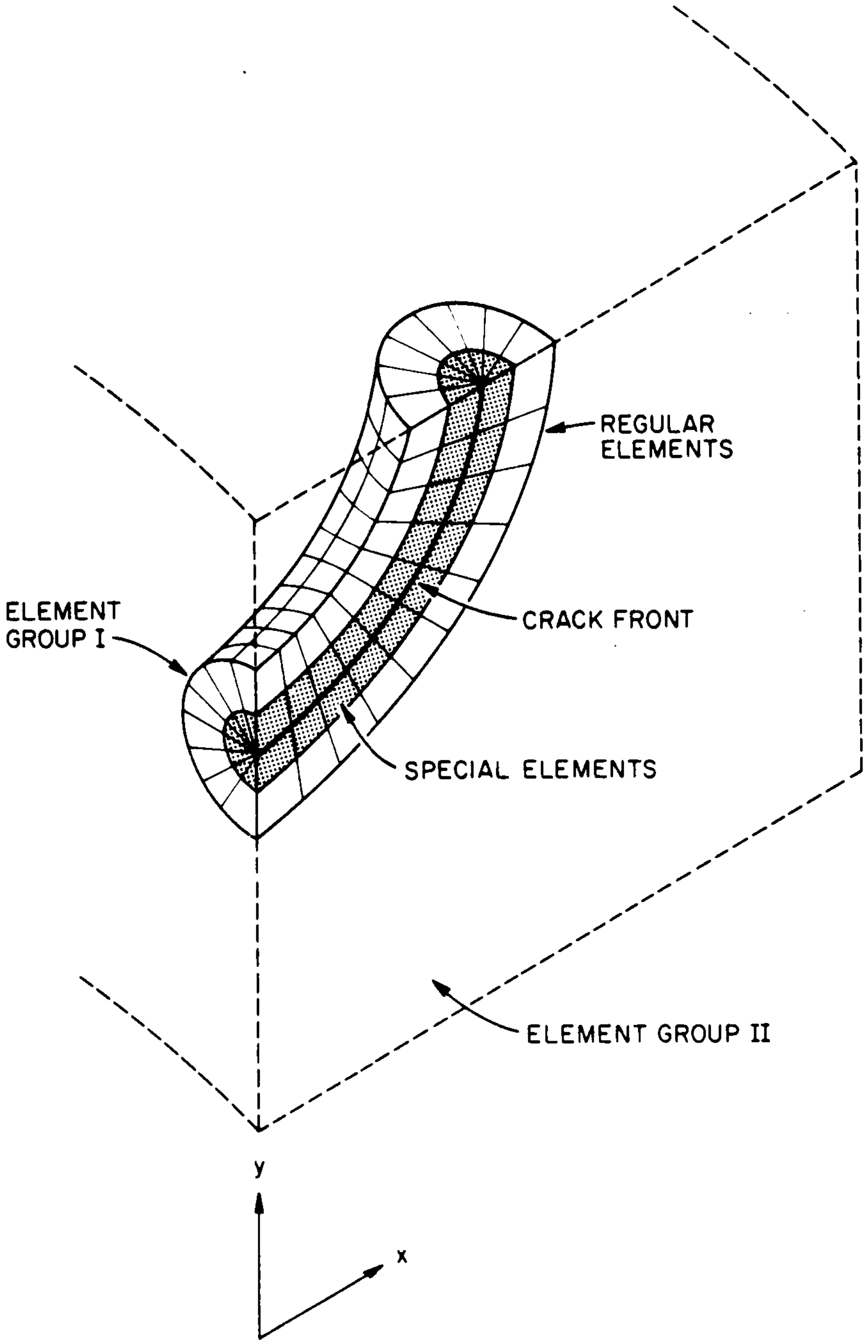

Figure A.1. Crack-tip region generated by ORMGEN-3D.

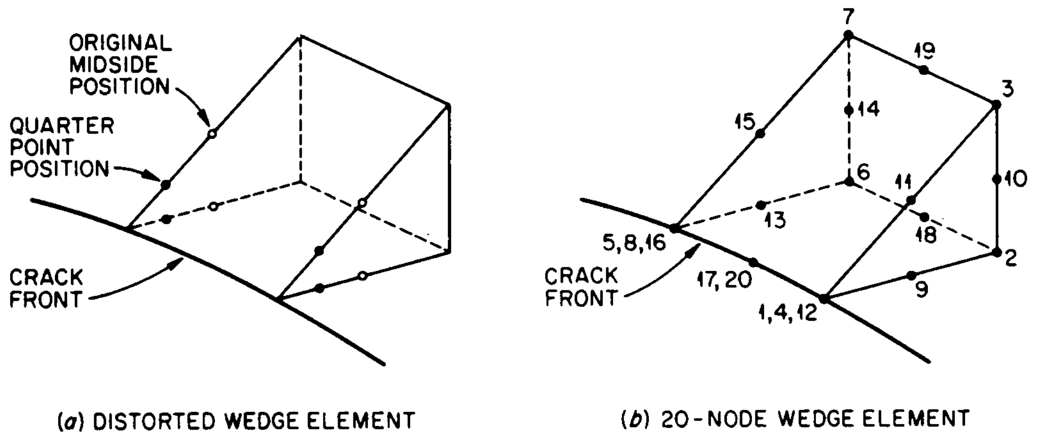

Figure A.2. Special crack-tip elements employed in ORMGEN-3D.

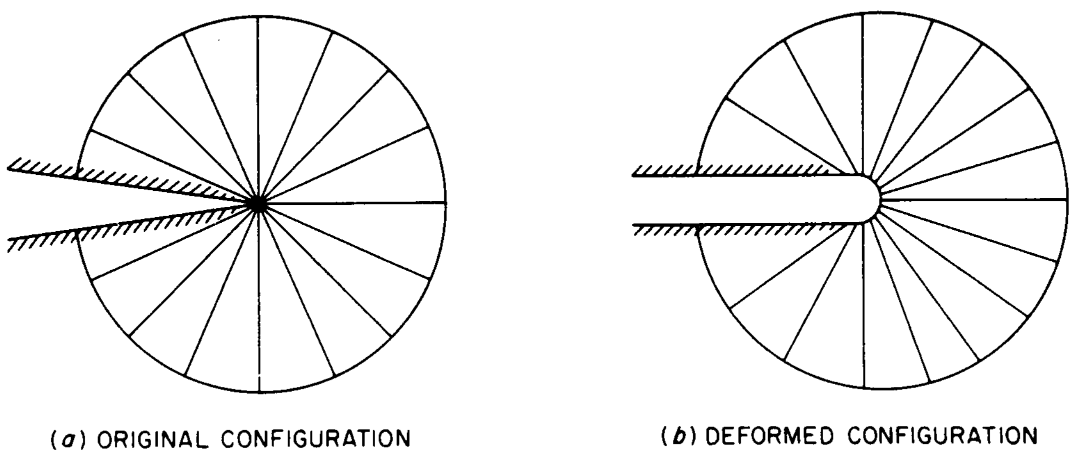

Figure A.3. Collapsed prism elements appropriate for nonlinear analysis.

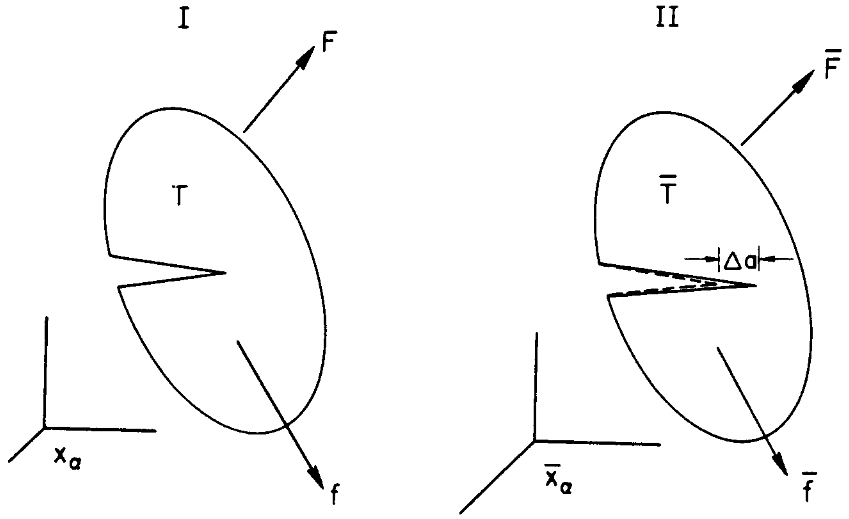

Figure A.4. Crack configuration before and after crack extension.

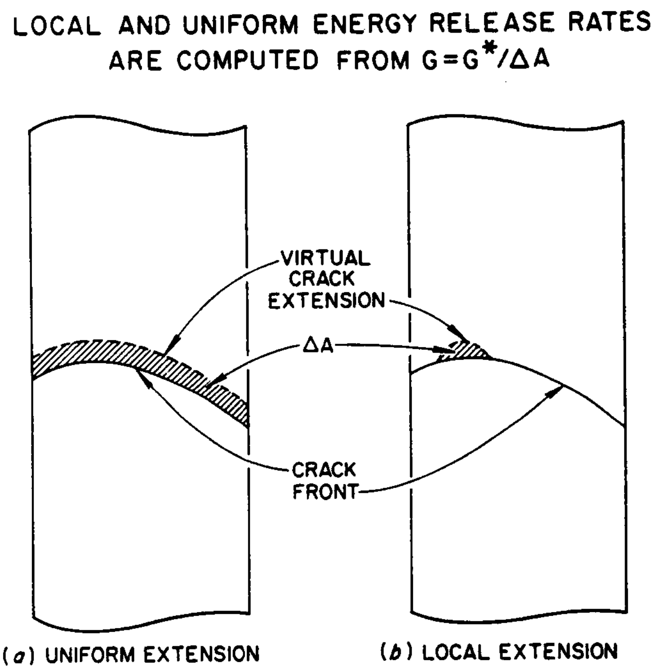

Figure A.5. Virtual crack extension for calculating energy release rate G_T for (a) uniform extension and (b) local extension.

VITA

Janis Keeney-Walker was born in Eugene, Oregon, on September 21, 1956. She moved to Watertown, New York in 1958 where she attended elementary schools and was graduated from Watertown High School in June 1974. The following September she entered the State University of New York at Plattsburgh, and in May 1978 she received a Bachelor of Arts degree in Anthropology. In the fall of 1978 she accepted employment with the Tennessee Department of Human Services in social work.

In the fall of 1980 she began study toward a Bachelor of Science degree in Chemical Engineering at the University of Tennessee, Knoxville. The degree was awarded in 1984. In the summer of 1984 she accepted employment with Martin Marietta Energy Systems, Incorporated, in the Engineering Mechanics Section of the Computer and Telecommunications Division. While working full time she began study toward a Master's degree. She received the Master's of Science degree with a major in Engineering Science in May 1990.

The author is a member of Tau Beta Pi, and the American Society for Testing and Materials (ASTM).